

American Journal of Science

DECEMBER 1966

THE JOIN FORSTERITE-DIOPSIDE-IRON OXIDE AND ITS BEARING ON THE CRYSTALLIZATION OF BASALTIC AND ULTRAMAFIC MAGMAS*

D. C. PRESNALL**

Department of Geochemistry and Mineralogy,
The Pennsylvania State University, University Park, Pennsylvania

ABSTRACT. The liquidus surface of the join forsterite-diopside-iron oxide has been studied by quenching techniques at a total pressure of 1 atm and at oxygen fugacities from $10^{-0.68}$ to 10^{-8} atm. At oxygen fugacities from $10^{-0.68}$ to 10^{-6} atm, the minimum liquidus temperature on the join forsterite-diopside-iron oxide remains nearly constant in temperature and composition at about 1300°C and 79 percent diopside, 21 percent iron oxide (total iron as FeO) by weight. Almost coincident with this minimum is a piercing point at which olivine, diopside, and spinel are in equilibrium. As oxygen fugacity decreases from $10^{-0.68}$ to 10^{-6} atm, the quantity $(\text{Fe}_2\text{O}_3)(100)/(\text{FeO} + \text{Fe}_2\text{O}_3)$ in the liquid at this piercing point decreases from 87.7 to 37.0 and the weight percent fayalite in the olivine in equilibrium with this liquid changes from 4 to 14 weight percent. At 10^{-6} atm oxygen fugacity, an additional piercing point occurs at which olivine, spinel, and magnesiowüstite are in equilibrium. At 10^{-8} atm oxygen fugacity, the primary phase field of spinel is absent, and no piercing points occur.

Comparison of published data on the chemistry of basaltic and ultramafic rocks with data on the join forsterite-diopside-iron oxide, inferred relationships in parts of the system $\text{CaO-MgO-FeO-Fe}_2\text{O}_3\text{-SiO}_2$ adjacent to this join, and previous data on the system $\text{MgO-FeO-Fe}_2\text{O}_3\text{-SiO}_2$ (Muan and Osborn, 1956) yields the following conclusions: (1) The Skaergaard intrusion represents the results of a close approach to fractional crystallization of an essentially anhydrous magma at constant total composition. In this situation, the oxygen fugacity of the magma would be controlled by the liquid and crystalline phases in equilibrium in the magma. (2) If basaltic magmas similar in composition to the initial Skaergaard magma have fractionally crystallized at relatively low pressures within the Earth's crust, and if liquids derived from this fractional crystallization have been produced at the surface as lavas, the oxygen fugacities of these basaltic magmas were controlled by oxidizing buffers. (3) The equilibrium diagrams support the hypothesis of Kuno (1950b) that in volcanic rocks, reaction rims consisting of both hypersthene and magnetite on olivine phenocrysts are the result of partial resorption of olivine by liquid. (4) At low pressures, peridotites can exist while partly liquid at temperatures as low as about 1250°C. Complete melting would require temperatures in the vicinity of 1700°C. (5) Fractional crystallization of ultramafic magma under conditions of buffered oxygen fugacity adequately explains the origin of the major ultramafic rock-types in the Duke Island ultramafic complex in Alaska.

INTRODUCTION

Several zoned ultramafic bodies in Alaska and British Columbia consist mainly of the minerals olivine, diopside, magnetite, and hornblende and are thought by field investigators to have crystallized from ultramafic magmas (Findlay, ms; Irvine, 1963; Ruckmick and Noble,

* Contribution no. 65-28, College of Mineral Industries, The Pennsylvania State University, University Park, Pennsylvania.

** Present address: Geophysical Laboratory, Carnegie Institution of Washington, Washington, D. C.

1959; Taylor and Noble, 1960). Inasmuch as about 90 percent of the composition of these ultramafic bodies consists of the five oxides CaO , MgO , FeO , Fe_2O_3 , and SiO_2 , an understanding of liquidus phase equilibria in the pertinent parts of this five-component system should allow a more certain interpretation of the manner in which these rocks were formed.

A knowledge of phase equilibria in the system $\text{CaO-MgO-FeO-Fe}_2\text{O}_3\text{-SiO}_2$ is also an important step toward an understanding of the crystallization behavior of basaltic magmas, for this system shows equilibrium relationships among the important basalt-forming minerals, olivine, diopsidic pyroxene, enstatitic pyroxene, and spinel.

The experimental work in this paper consists of a determination of the liquidus surface of the join forsterite-diopside-iron oxide at $10^{-0.68}$ atm oxygen fugacity, at the oxygen fugacity produced by the equilibrium decomposition of pure CO_2 , at 10^{-6} atm oxygen fugacity, and at 10^{-8} atm oxygen fugacity (see fig. 1). This study is thus an exploration into that part of the system $\text{CaO-MgO-FeO-Fe}_2\text{O}_3\text{-SiO}_2$ that applies most directly to the ultramafic rocks in Alaska and British Columbia but also partly to problems of crystallization of basaltic magmas. Since all experiments were performed at a total pressure of 1 atm, the geologic applications are limited to crystallization processes taking place at low pressures in the Earth's crust.

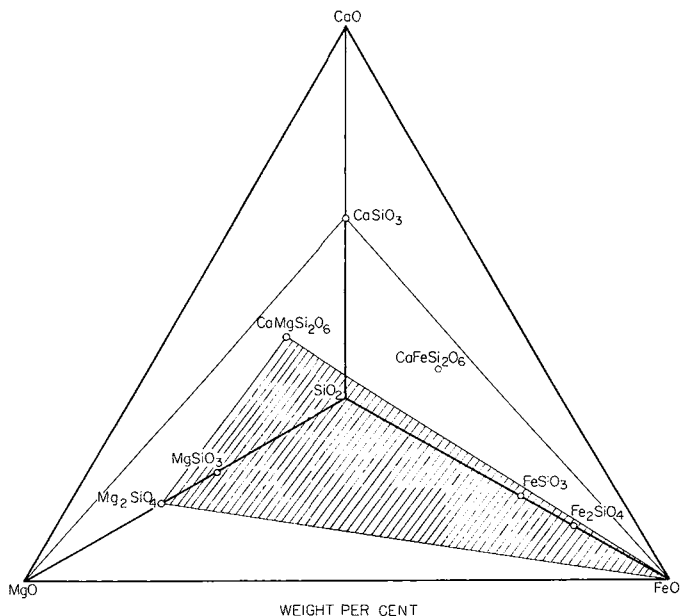


Fig. 1. The tetrahedron CaO-MgO-FeO-SiO_2 . The apex labeled FeO indicates total iron calculated as FeO . The join studied in the present investigation is shown as a ruled surface.

ACKNOWLEDGMENTS

In particular, I thank E. F. Osborn, who proposed the general area of study, for stimulating discussions, helpful suggestions, and encouragement throughout the work. His writings on the crystallization of basaltic magma provided the initial stimulus for the ideas presented here on the same subject. I also wish to thank C. O. Ingamells for generously providing space and equipment in his laboratory on several occasions and for many suggestions that led directly to significant improvements in the iron determinations reported here. I am indebted to Takashi Katsura for additional suggestions on analytical procedures, to J. W. Greig for guidance in the preparation of polished sections and for helpful discussions regarding experimental procedures, to Ikuo Kushiro for translations of Japanese literature, to T. N. Irvine, D. H. Lindsley, A. J. Naldrett, P. L. Roeder, and R. W. Taylor for stimulating discussions, and to Felix Chayes and Marjorie Hooker for permitting me access to their personal files of rock analyses. The literature search for chemical analyses of lavas would not have been made without their compilations. I am indebted to E. C. Hansen, T. N. Irvine, D. H. Lindsley, A. J. Naldrett, E. F. Osborn, D. R. Wones, and H. S. Yoder, Jr., for critical review of the manuscript. Much of the writing and the literature search for chemical analyses of lavas were done at the Geophysical Laboratory, Carnegie Institution of Washington. Funds for experimental apparatus were provided by the American Iron and Steel Institute and the National Science Foundation. These two organizations and the Corning Glass Works supplied additional financial support in the form of fellowships.

EXPERIMENTAL METHOD

The quenching technique (Shepherd, Rankin, and Wright, 1909, p. 308), modified to permit control of the oxygen fugacity, was employed in determining liquidus surfaces at 1 atm total pressure. Open-topped, folded platinum foil envelopes containing the desired charges were suspended in a vertical quench-furnace until equilibrium among the various phases was reached. Phases in quenched samples were identified by microscopic examination in both reflected and transmitted light and by powder X-ray diffraction. After the liquidus temperature for a given mixture was determined, another sample of the same mixture was held at this temperature, quenched, and analyzed for FeO and total iron. The oxygen fugacity was controlled by equilibrating the samples with air, CO₂, or a mixture of CO₂ and H₂ supplied by a gas mixer. Compositions of olivines were determined by a combination of optical and X-ray methods. Compositions of diopsides, spinels, and magnesio-wüstites were not determined. Further details on the experimental method are given in appendix A.

REPRESENTATION OF THE EQUILIBRIUM DIAGRAMS

In the study of iron-bearing ternary and quaternary oxide systems at a total pressure of 1 atm, it has been common to remove one

degree of freedom by equilibrating the condensed phases with a continuous flow of gas whose oxygen fugacity is independent of temperature. The resulting equilibrium diagrams have been represented by showing the phase equilibrium relations on a chosen join in which the iron is in an arbitrarily fixed state of oxidation. For example, in the system MgO-iron oxide-SiO₂ at 10^{-0.68} atm oxygen fugacity, Muan and Osborn (1956, fig. 5) found different Fe₂O₃/FeO ratios for different mixtures at their liquidus temperatures. For purposes of representation, they converted all iron oxide to Fe₃O₄, recalculated the oxide percentages to 100 percent, and plotted the resulting compositions on the join MgO-Fe₃O₄-SiO₂. This procedure is equivalent to projecting all liquid compositions onto the join MgO-Fe₃O₄-SiO₂ along lines defined by the compositions in question and the oxygen apex of the tetrahedron Mg-Fe-Si-O. These lines are the "oxygen reaction lines" of Muan (1958, p. 194) and the "total composition lines" of Osborn (1959, p. 613).¹

In figure 2A, the system MgO-iron oxide-SiO₂ is shown with all iron calculated as FeO so that compositions of pyroxenes and olivines containing iron can be read directly from the diagram. Figure 2A has the appearance of the equilibrium diagram of a ternary system but actually shows equilibrium relations at 10^{-0.68} atm oxygen fugacity in the quarternary system MgO-FeO-Fe₂O₃-SiO₂. This diagram can be used for deducing liquid crystallization paths at 10^{-0.68} atm oxygen fugacity just as if it were the diagram of a ternary system; no reference to the tetrahedron MgO-FeO-Fe₂O₃-SiO₂ is necessary. (For an example of another system treated in this way, see Muan and Sōmiya, 1960.) As equilibrium crystallization proceeds at constant oxygen fugacity, the oxygen content of the total mixture changes along its total composition line in the tetrahedron MgO-FeO-Fe₂O₃-SiO₂, but the projected total composition remains at the same point on the plane of projection. That is, the starting composition, in terms of SiO₂, MgO, and total iron oxide as FeO, does not move on the join MgO-FeO-SiO₂ as the oxygen content of the mixture varies during cooling. Thus, all the usual geometric devices for deducing liquid crystallization paths in a ternary system can be used.

When using the projected diagram, MgO-FeO-SiO₂, to determine relative proportions of phases in equilibrium, direct measurement does not yield the true proportions of phases but rather the proportions that would exist if all iron in each of the phases in equilibrium were present as FeO. However, if the amount of Fe₂O₃ in each phase were known, then the apparent proportion of each of these phases as read from the diagram could be recalculated to its true proportion by using appropriate conversion factors. The calculation of the total composition of the mixture (that is, the position of the mixture on its total com-

¹ Hereafter, when a composition is spoken of as projected onto a join, it will be understood that the projection is performed along the total composition line passing through the composition in question.

position line) would follow immediately. In order to make these calculations, it would be necessary to show three sets of lines on the liquidus surface in addition to liquidus isotherms. One of these sets would be fractionation curves (Bowen, 1941), and the other two would be contours showing $\text{Fe}_2\text{O}_3/\text{FeO}$ ratios of liquids and $\text{Fe}_2\text{O}_3/\text{FeO}$ ratios of crystalline phases in equilibrium with these liquids. The $\text{Fe}_2\text{O}_3/\text{FeO}$ ratios of liquids have been shown in this way by Muan and Osborn (1956, fig. 5).

Thus, for a four-component oxide system containing iron, all the liquidus equilibrium relationships at a constant oxygen fugacity can be shown on a projected triangular diagram. When the above treatment is extended to a five-component oxide system containing iron, the equilibrium relationships at a constant oxygen fugacity are represented in a tetrahedron, and total iron oxide is calculated as FeO and plotted at one apex. Again, no compositional information at this oxygen fugacity need be sacrificed by projecting into the tetrahedron. The data on $\text{Fe}_2\text{O}_3/\text{FeO}$ ratios of the various phases in equilibrium at liquidus temperatures could be shown by contour surfaces passing through the various primary phase volumes. The projected diagram at constant oxygen fugacity would look like a quaternary system and could be treated as such when deducing crystallization paths at constant oxygen fugacity. As before, true relative proportions of phases could be calculated using the contoured data on $\text{Fe}_2\text{O}_3/\text{FeO}$ ratios of phases.

The equilibrium diagrams that follow are projected in the manner described above. All iron is calculated as FeO so that compositions of olivines and pyroxenes can be read directly from the diagrams without recalculation. Some of the projected diagrams to be discussed below do not show phase relationships at constant oxygen fugacity but instead show phase relationships in equilibrium with a gas of constant bulk composition. In each case, the oxygen fugacity imposed on the condensed phases by this gas varies continuously with temperature but is defined at any given temperature by the equilibrium constants for the gas reactions involved. Thus, in all of these diagrams, the principles discussed above are fully applicable.

THE LIMITING JOINS

The join forsterite-diopside-iron oxide is not bounded on any of its sides by binary systems. Equilibrium relationships on the limiting join forsterite-iron oxide at various oxygen fugacities can be understood from figure 2. Figure 2B does not show relationships at constant oxygen fugacity because pure CO_2 decomposes at high temperatures according to the reaction $\text{CO}_2 = \text{CO} + \frac{1}{2} \text{O}_2$, and the oxygen fugacity at elevated temperatures is determined by the equilibrium constant for this reaction. The exact oxygen fugacity at a given temperature can be found from figure 9. The boundary curve between olivine and magnesiowüstite in figure 2D has not been drawn at high temperatures because this curve intersects the primary phase volume of metallic iron. The phase

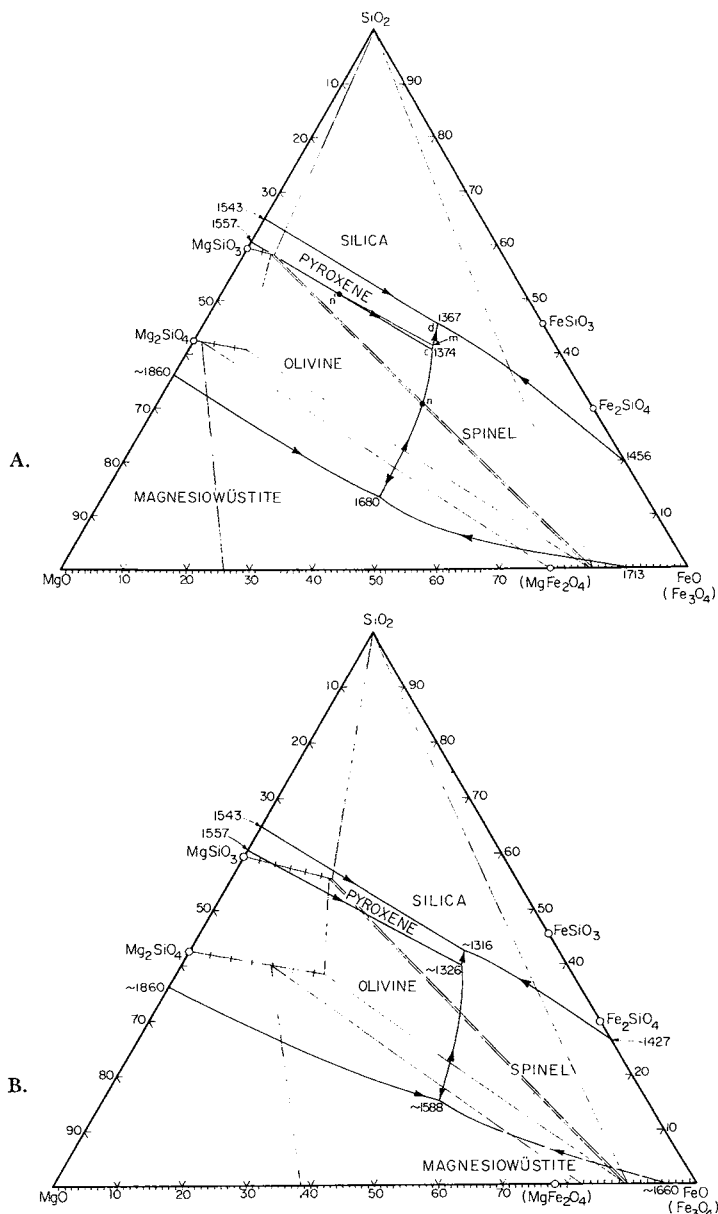
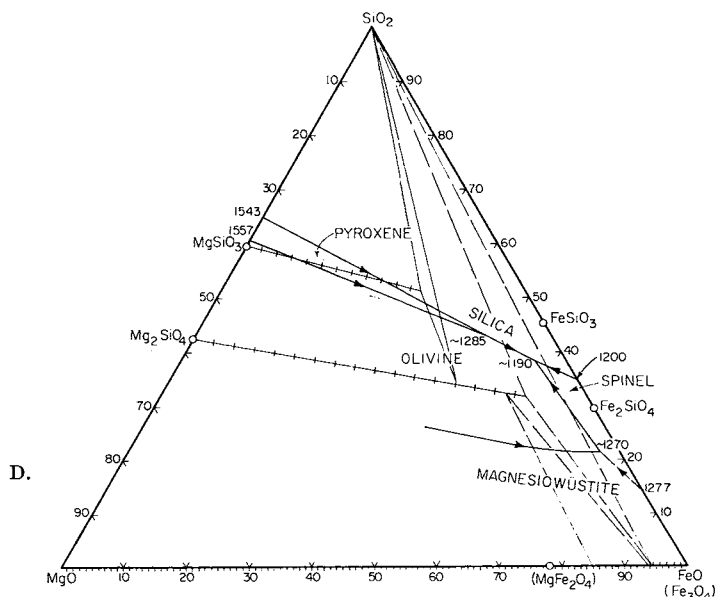
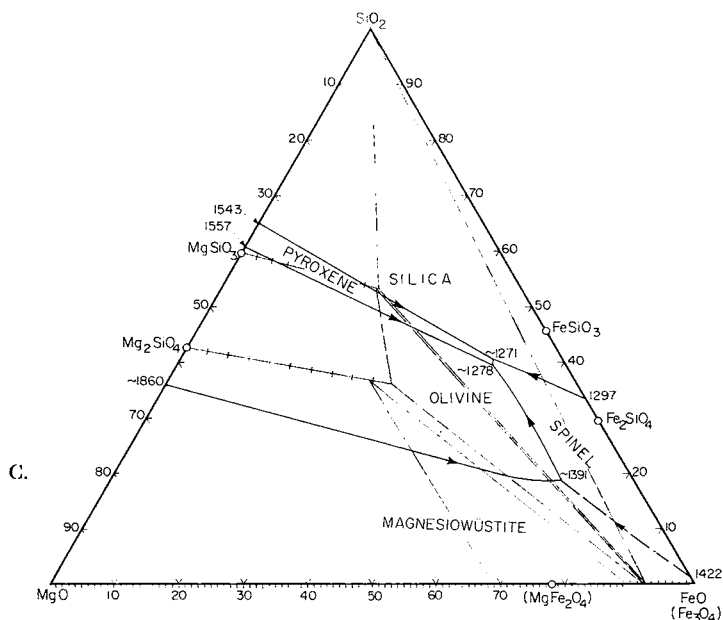


Fig. 2. The system MgO-iron oxide-SiO₂ at 10^{-0.65} atm oxygen fugacity (A), at the oxygen fugacity produced by the equilibrium decomposition of pure CO₂ (B), at 10⁻⁸ atm oxygen fugacity (C), and at 10⁻⁸ atm oxygen fugacity (D). All diagrams are drawn in weight percent. Diagram A is redrawn after Muan and Osborn (1965, fig. 5) and Phillips, Sömiya, and Muan (1961, fig. 1). Diagrams B, C, and D are interpolated from diagrams and data by Muan and Osborn (1956). Medium-weight lines are liquidus boundary curves with arrows pointing in directions of decreasing temperature. Light-weight lines connect compositions of coexisting crystalline phases at solidus temperatures. These lines outline the shape of the solidus surface; the temperature of a three-phase triangle is that of its corresponding liquidus invariant point, and the temperature variation across a two-phase area is given by the temperature variation along its corresponding liquidus boundary curve. Compounds whose compositions have been



projected onto the join MgO-FeO are shown in parentheses. Numbers beside invariant points are temperatures in degrees C. The extents of the magnesiowüstite and spinel solid solutions are indicated by short graduations extending below and above the base line of the triangle, respectively. These graduations are spaced every 5 percent of each end member for spinel and every 1 percent for magnesiowüstite. Similar graduations for the olivine and pyroxene solid solutions are spaced every 5 percent. In diagrams B, C, and D, the maximum amounts of solid solution for magnesiowüstite and spinel are inferred. In diagrams C and D, the boundary curve between magnesiowüstite and olivine has been curved slightly so as to correlate better with the present data. Liquidus isotherms, the boundary curve between tridymite and cristobalite, and the region of immiscibility in the field of silica are omitted.

equilibrium relations at temperatures above this intersection are not usefully represented or discussed here, and the boundary curve is simply stopped at the approximate inferred location of the intersection. Recent data (Speidel, ms) indicate that the inferred compositions of spinels shown at solidus temperatures in figure 2 are too rich in magnesium. Tie-lines from spinel compositions will be shifted to the right by these new data, but the general appearance of the diagrams will not change.

Bowen (1914, fig. 3) originally drew the limiting join forsterite–diopside as a binary system with a eutectic and with no solid solutions in either forsterite or diopside. Osborn and Muan (1960) inferred that this join shows ternary behavior due to the presence of calcium in forsterite. Kushiro and Schairer (1963) experimentally confirmed this inference and, in addition, found solid solution in diopside and a maximum on the diopside liquidus.

Figure 3 shows the limiting join diopside–iron oxide at $10^{-0.68}$ atm oxygen fugacity. For oxygen fugacities other than $10^{-0.68}$ atm, no data have been collected on this join below liquidus temperatures.

THE LIQUIDUS SURFACES

Figure 4A shows the liquidus surface of the join forsterite–diopside–iron oxide at $10^{-0.68}$ atm oxygen fugacity. The data on which this diagram is based are given in appendix B. The diagram is not ternary because compositions of crystalline phases do not lie on the join. Contours of the quantity $(\text{Fe}_2\text{O}_3)_{(100)} / (\text{FeO} + \text{Fe}_2\text{O}_3)$ in the part of the diagram that is low in FeO are inferred. Mixtures in this region of the diagram were analyzed for iron, but reproducible determinations of FeO could not be obtained (see appendix A for further discussion).

No direct comparisons can be made between the data for the quantity $(\text{Fe}_2\text{O}_3)_{(100)} / (\text{FeO} + \text{Fe}_2\text{O}_3)$ plotted in figure 4A and similar data of previous investigators. However, some comparisons based on extra-

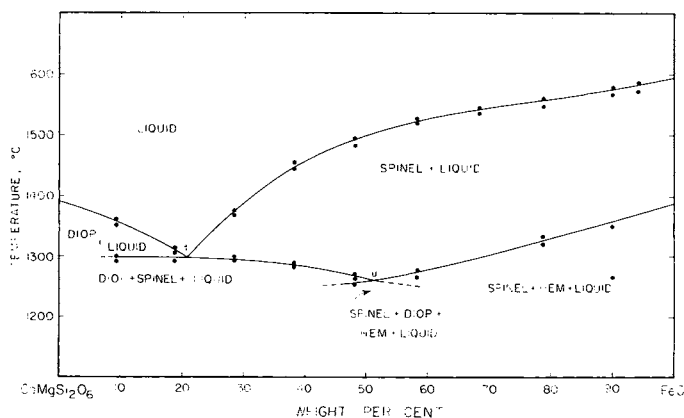


Fig. 3. The join diopside–iron oxide at $10^{-0.68}$ atm oxygen fugacity. Solid circles are experimental points listed in appendix B. DIOP = diopside, HEM = hematite.

polations are possible. Muan and Osborn (1956), in their study of the system MgO-iron oxide-SiO₂ at 10^{-0.68} atm oxygen fugacity, determined FeO and total iron in mixtures quenched from their liquidus temperatures. They did not analyze mixtures on the join forsterite-iron oxide, but they extrapolated to this join from data in other parts of the diagram (see their fig. 5). Data in the present work are also extrapolated to the join forsterite-iron oxide (fig. 4A). In the magnesioferrite (here referred to as spinel) field of the diagram by Muan and Osborn, Fe₂O₃ decreases relative to FeO when moving along the join forsterite-iron oxide toward forsterite. Data from the present investigation, however, indicate that Fe₂O₃ increases relative to FeO under the same conditions (fig. 4A). The maximum discrepancy occurs at the boundary curve between spinel and olivine. At this point, Muan and Osborn show a value for Fe₂O₃/FeO by weight of about 1.34, which, when converted to the quantity (Fe₂O₃)(100)/(FeO + Fe₂O₃), is 57.3. This is to be compared with the value 81.7, taken from figure 4A. The reason for this difference is unknown. It cannot be accounted for by slight errors in extrapolating to the join forsterite-iron oxide. The belief that the iron determinations in this work are correct is supported by close agreement with the data of Darken and Gurry (1946, table 1). The present data for the quantity (Fe₂O₃)(100)/(FeO + Fe₂O₃) along the join diopside-iron oxide extrapolate to the value 74.2 for pure iron oxide at its liquidus temperature, 1595°C; at this same temperature, Darken and Gurry obtained the value 3.529 for the quantity (Fe⁺⁺ + Fe⁺⁺⁺)/Fe⁺⁺, which, when converted to the quantity (Fe₂O₃)(100)/(FeO + Fe₂O₃), is 73.8.

Figures 4B to D show the liquidus surface of the join forsterite-diopside-iron oxide at the oxygen fugacity produced by the equilibrium decomposition of pure CO₂, at 10⁻⁶ atm oxygen fugacity, and at 10⁻⁸ atm oxygen fugacity, respectively. Data for these diagrams are given in appendices C, D, and E. Pure CO₂ was used in determining figure 4B because the ratio CO₂/H₂ required to yield the desired oxygen fugacity, about 10⁻³ atm, is so large that it is difficult to achieve accurately with a gas-mixer. The high temperature part of figure 4D has been omitted because this diagram intersects the primary phase field of metallic iron, as discussed earlier in reference to figure 2D. The line of intersection has not been determined, so the boundary curve and liquidus isotherms are merely stopped at the approximate inferred location of the line.

COMPOSITIONS OF CRYSTALLINE PHASES

In the system CaO-MgO-FeO-Fe₂O₃-SiO₂, there would seem to be the possibility of forming olivines near the join forsterite-fayalite that contain calcium, ferric iron, or both, in addition to magnesium and ferrous iron. Since Takashi Katsura (oral communication, 1962) found no ferric iron in fayalite in his investigations in the system FeO-Fe₂O₃-SiO₂, it is assumed that none exists in olivine when the additional

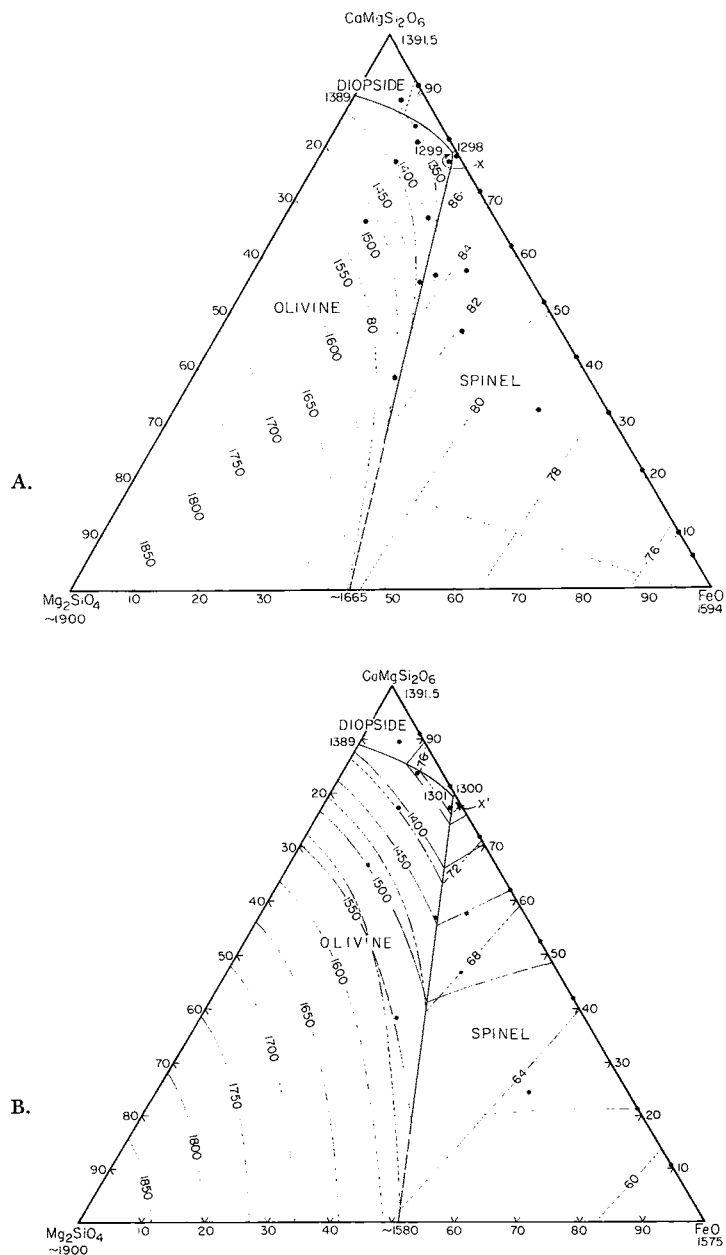
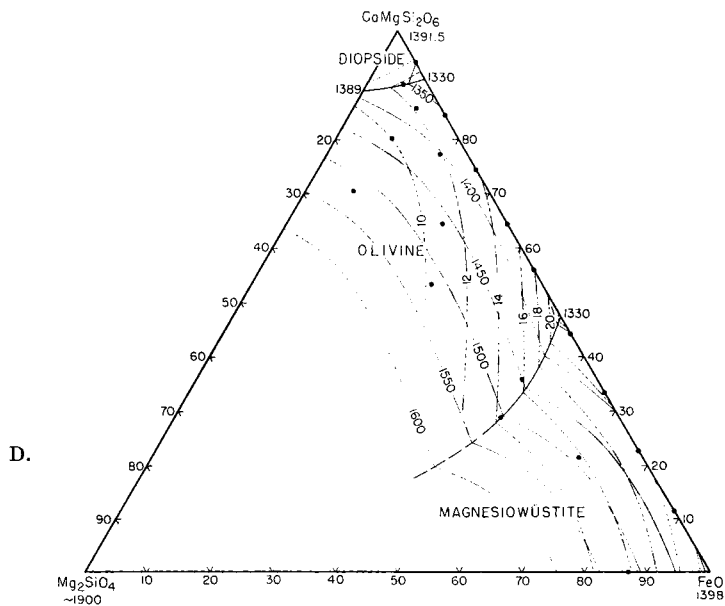
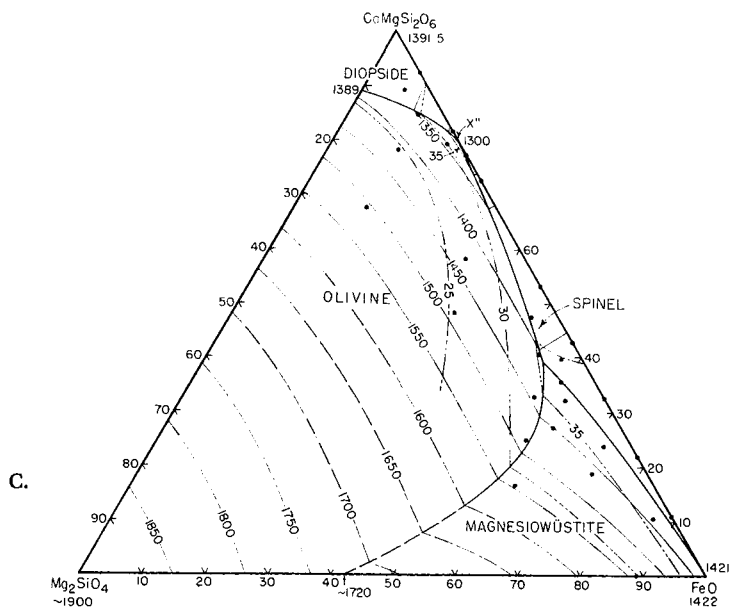


Fig. 4. The join forsterite-diopside-iron oxide at $10^{-0.68}$ atm oxygen fugacity (A), at the oxygen fugacity produced by the equilibrium decomposition of pure CO_2 (B), at 10^{-8} atm oxygen fugacity (C), and at 10^{-8} atm oxygen fugacity (D). Filled circles are compositions of mixtures studied. Medium-weight lines (dashed where approximately



located) that separate the primary phase fields are not univariant lines because this join is not ternary. Light-weight long and short dashed lines (continuously short dashed where approximately located) are contours of the quantity $(\text{Fe}_2\text{O}_3)/(100/(\text{FeO} + \text{Fe}_2\text{O}_3))$ on the liquidus surface.

oxides CaO and MgO are added to the system. If this assumption is granted and if the compositions of olivine solid solutions do not otherwise deviate from the orthosilicate join, then two parameters are sufficient to fix an olivine composition in the five-component system. Two such parameters are d_{130} and the β refractive index.

Figure 5 shows inferred contours of d_{130} and β refractive index in the vicinity of the forsterite apex of the orthosilicate join, Mg_2SiO_4 – Ca_2SiO_4 – Fe_2SiO_4 . The contours are based on data for the binary solid solutions, and the properties are assumed to vary linearly with composition on the ternary mole percent diagram. Justifications for this assumption are: (1) the linear variation of refractive index versus mole percent composition found by Bowen and Schairer (1935, fig. 25) for forsterite-fayalite solid solutions and by Bowen, Schairer, and Posnjak (1933a, fig. 5) for fayalite-kirschsteinite solid solutions; and (2) the linear variation of d_{130} with mole percent composition found by Yoder and Sahama (1957, fig. 1) for natural forsterite-fayalite solid solutions.

In order to test for the presence of calcium, samples were held well below their liquidus temperatures so as to produce sufficient olivine for precise measurement of d_{130} as well as the β refractive index. Table 1 lists measured values of d_{130} and β refractive index for three olivines. Rows 3 and 4 of this table show that if calcium is assumed to be absent, the amounts of fayalite in the olivines are quite different depending

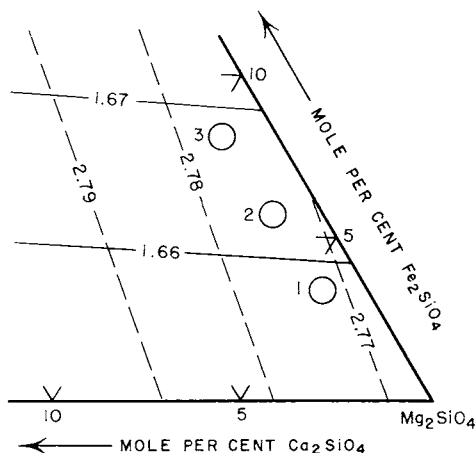


Fig. 5. Compositions of olivines. Solid lines are contours of β refractive index and dashed lines are contours of d_{130} in Å. Open circles are olivine compositions determined by measuring both the d_{130} and the β refractive index. The estimated uncertainty in composition, assuming that the contours are correct, is indicated by the size of the circles. Numbers beside the circles key the compositions to table 1. The contours of d_{130} are based on the data of Yoder and Sahama (1957, p. 186) for forsterite and fayalite and Sahama and Hytonen (1958, p. 869) for monticellite and kirschsteinite. The contours of β refractive index are based on the data of Bowen and Schairer (1935, p. 196) for the forsterite-fayalite solid solution series, Ferguson and Merwin (1919, p. 92) for monticellite, and Bowen, Schairer, and Posnjak (1933a, fig. 5) for kirschsteinite.

TABLE 1
Compositions of olivines based on β refractive indices and d_{130}

Sample number	1	2	3
n_β of olivine	1.658	1.663	1.668
d_{130} of olivine (\AA)	2.772	2.774	2.776
Mole percent fayalite using n_β^*	3	6	8
Mole percent fayalite using d_{130}^{**}	10	13	16
Olivine composition (mole percent) from figure 5†	$\text{Fo}_{10}\text{Fa}_3\text{La}_1$	$\text{Fo}_{13}\text{Fa}_6\text{La}_1$	$\text{Fo}_{16}\text{Fa}_8\text{La}_1$
Composition of mixture (wt percent)‡	$\begin{cases} \text{Mg}_2\text{SiO}_4 & 20.5 \\ \text{CaMgSi}_2\text{O}_6 & 66.4 \\ \text{total Fe as FeO} & 13.1 \end{cases}$	$\begin{cases} 20.5 \\ 66.7 \\ 12.8 \end{cases}$	$\begin{cases} 21.7 \\ 70.5 \\ 7.8 \end{cases}$
Temp ($^\circ\text{C}$)	1309	1309	1338
Time (hours)	11	20	28
Oxygen fugacity (atm)	$10^{-0.68}$	$10^{-3.39}$	10^{-8}
Mixing ratio, CO_2/H_2	—	pure CO_2	4.74
Phases present¶	ol + diop + l	ol + diop + l	ol + l

* Using the optical data of Bowen and Schairer (1935, fig. 25) for synthetically made forsterite-fayalite solid solutions.

** Using the equation of Yoder and Sahama (1957, p. 486) for synthetically made forsterite-fayalite solid solutions.

† $\text{Fo}_x\text{Fa}_y\text{La}_z = x$ percent Mg_2SiO_4 , y percent Fe_2SiO_4 , z percent Ca_2SiO_4 .

‡ The compositions shown are for these mixtures at their liquidus temperatures as given in appendices B, C, and D.

¶ ol = olivine, diop = diopside, l = liquid.

on whether the β refractive index or the d_{130} value is used. The discrepancies can be explained by small amounts of Ca_2SiO_4 in the olivines; the resulting ternary solid solutions are then determined by the intersections of the appropriate n_β and d_{130} contours. The three compositions so determined are given in row 5 of table 1 and shown graphically as points 1, 2, and 3 in figure 5. Although these determinations indicate the amount of calcium present in the olivines, they are not otherwise useful because these olivines are in equilibrium with liquids whose precise compositions are unknown.

In order to measure compositions of olivines in equilibrium with liquids lying essentially on the join forsterite-diopside-iron oxide, mixtures were held at temperatures only slightly below their liquidus temperatures. This procedure did not yield sufficient amounts of olivine for measurements of d_{130} ; however, figure 5 shows that for an olivine containing a small amount of Ca_2SiO_4 , the fayalite percentage can be determined with only slight uncertainty by measuring just the β refractive index. Table 2 shows three determinations of fayalite percentage by this method. It is assumed, based on the data in table 1, that these olivines contain very small amounts of Ca_2SiO_4 . The three olivine compositions

TABLE 2

Compositions of olivines in equilibrium with liquids
on the join forsterite-diopside-iron oxide

n_β of olivine	1.657	1.666	1.673
Amount of fayalite*	$\left\{ \begin{array}{l} \text{mole percent} \\ \text{wt percent} \end{array} \right.$	$\left\{ \begin{array}{l} 3 \\ 4 \end{array} \right.$	$\left\{ \begin{array}{l} 7 \\ 10 \end{array} \right.$
Oxygen fugacity (atm)	$10^{-0.63}$	$10^{-3.41}$	10^{-6}
Approximate composition of equilibrium liquid phase	x (fig. 4A)	x' (fig. 4B)	x'' (fig. 4C)
Composition of mixture (wt percent, iron oxides by analysis)	$\left\{ \begin{array}{l} \text{Mg}_2\text{SiO}_4 \\ \text{CaMgSi}_2\text{O}_6 \\ \text{Total Fe as FeO}^{**} \\ (\text{Fe}_2\text{O}_3)(100) \\ \text{FeO} + \text{Fe}_2\text{O}_3 \end{array} \right.$	$\left\{ \begin{array}{l} 2.0 \\ 77.0 \\ 21.0 \\ 20.9 \\ 77.1 \end{array} \right.$	$\left\{ \begin{array}{l} 2.0 \\ 77.4 \\ 20.6 \\ *** \end{array} \right.$
Liquidus temp of mixture ($^{\circ}\text{C}$, from appendices B, C, and D)	1321	1320	1354
Sample for measurement of n_β^\dagger	$\left\{ \begin{array}{l} \text{temp } (^{\circ}\text{C}) \\ \text{time (hours)} \end{array} \right.$	$\left\{ \begin{array}{l} 1313 \\ 18 \end{array} \right.$	$\left\{ \begin{array}{l} 1305 \\ 22 \end{array} \right.$
Sample for analysis ‡	$\left\{ \begin{array}{l} \text{temp } (^{\circ}\text{C}) \\ \text{time (hours)} \end{array} \right.$	$\left\{ \begin{array}{l} 1313 \\ 24 \end{array} \right.$	$\left\{ \begin{array}{l} 1297 \\ 21 \end{array} \right.$
Mixing ratio, C_2/H_2	—	pure CO_2	70.6
Phases present §	ol + sp + l	ol + l \parallel	ol + diop (trace) + sp (trace) + l

* Using the optical data of Bowen and Schairer (1935, fig. 25), for synthetically made forsterite-fayalite solid solutions.

** Total Fe as FeO =

$$\left(\frac{\text{g FeO} + (\text{g Fe}_2\text{O}_3)(0.8998)}{\text{g FeO} + (\text{g Fe}_2\text{O}_3)(0.8998) + \text{wt of all other oxides}} \right) (100).$$

*** This sample was inadvertently oxidized during quenching and yielded an anomalously low FeO determination.

† The samples for determination of FeO and total iron were entirely consumed, and it was therefore necessary to make separate, duplicate samples for measurement of the β refractive indices of the olivines.

‡ ol = olivine, sp = spinel, diop = diopside, l = liquid.

\parallel This same mixture held in CO_2 at 1301°C for 20 hours showed the phases olivine, diopside, spinel, and liquid. The composition of the liquid is therefore very close to point x' in figure 4B.

given in this table are in equilibrium with liquids essentially at points x , x' , and x'' in figure 4.

One might argue that the determinations of β refractive index are uncertain due to the difficulty of obtaining an olivine edge completely free of attached glass. However, for all of the samples except the one made at 10^{-8} atm oxygen fugacity (see table 1), the glass was colored distinctly brown whereas the olivine grains were colorless. Furthermore, all of the values were verified by measurements on at least two carefully selected grains. Still, thin layers of glass might have remained undetected, so there is some possibility of error due to this effect. For

all the samples for which there are data in tables 1 and 2, except the one at 10^{-8} atm oxygen fugacity in table 1, the refractive index of the glass is greater than the β refractive index of the olivine. Thus, a compound edge consisting of olivine and glass would give an erroneously high β refractive index for the olivine, which would yield an erroneously high fayalite percentage. Therefore, this error would not affect the previous conclusion that Ca_2SiO_4 is present in the olivines. The determined amount of Ca_2SiO_4 simply would be less than that actually present. For the sample made at 10^{-8} atm oxygen fugacity in table 1, the index of refraction of the glass is less than the β refractive index of the olivine, and the determined amount of Ca_2SiO_4 would be greater than that actually present.

Compositions of diopsides and spinels were not determined. However, the spinels must consist primarily of compositions along the join between Fe_3O_4 and MgFe_2O_4 , the proportion of magnetite being greater at lower oxygen fugacities. Compositions of diopsides must be near the join $\text{CaMgSi}_2\text{O}_6$ – $\text{CaFeSi}_2\text{O}_6$, and may contain small amounts of ferric iron.

THE JOIN CaSiO_3 – MgO –IRON OXIDE– SiO_2 AS A FUNCTION OF OXYGEN FUGACITY

The diagrams presented above for the join forsterite–diopside–iron oxide at different oxygen fugacities are more easily understood by considering probable relationships in adjacent parts of the system CaO – MgO – FeO – Fe_2O_3 – SiO_2 . In the treatment that follows, the tetrahedron CaSiO_3 – MgO –iron oxide– SiO_2 in figure 1 is removed from the tetrahedron CaO – MgO –iron oxide– SiO_2 and shown in figure 6 as a series of separate equilateral tetrahedra, presented in order of decreasing oxygen fugacity.

In figure 6, liquidus boundary curves in the faces of the tetrahedra form limits for divariant surfaces within the tetrahedra. Similarly, liquidus invariant points in the faces of the tetrahedra form limits for univariant lines inside the tetrahedra. Each of these univariant lines is the intersection of three divariant surfaces and defines the compositions of liquids in equilibrium with three crystalline phases. In figures 6A to C, three proposed invariant points are shown inside each tetrahedron; at each of these points, four crystalline phases are in equilibrium with liquid. At points *b*, *b'*, and *b''*, the crystalline phases are diopside, akermanite, olivine, and spinel; at points *d*, *d'*, and *d''*, the phases are diopside, protoenstatite, olivine, and spinel; and at points *e*, *e'*, and *e''*, they are diopside, protoenstatite, spinel, and silica. This arrangement of invariant points is the same as that proposed by Osborn (1962a, fig. 4). However, only the existence and partial location of univariant lines *b*–*d*, *b'*–*d'*, and *b''*–*d''* have been established by the present data; it is not possible to be certain that all three of the proposed invariant points shown in each of these tetrahedra exist. Arrows on univariant lines have been omitted where the direction of falling temperature is uncertain. In each tetrahedron, the curved lines on the join forsterite–

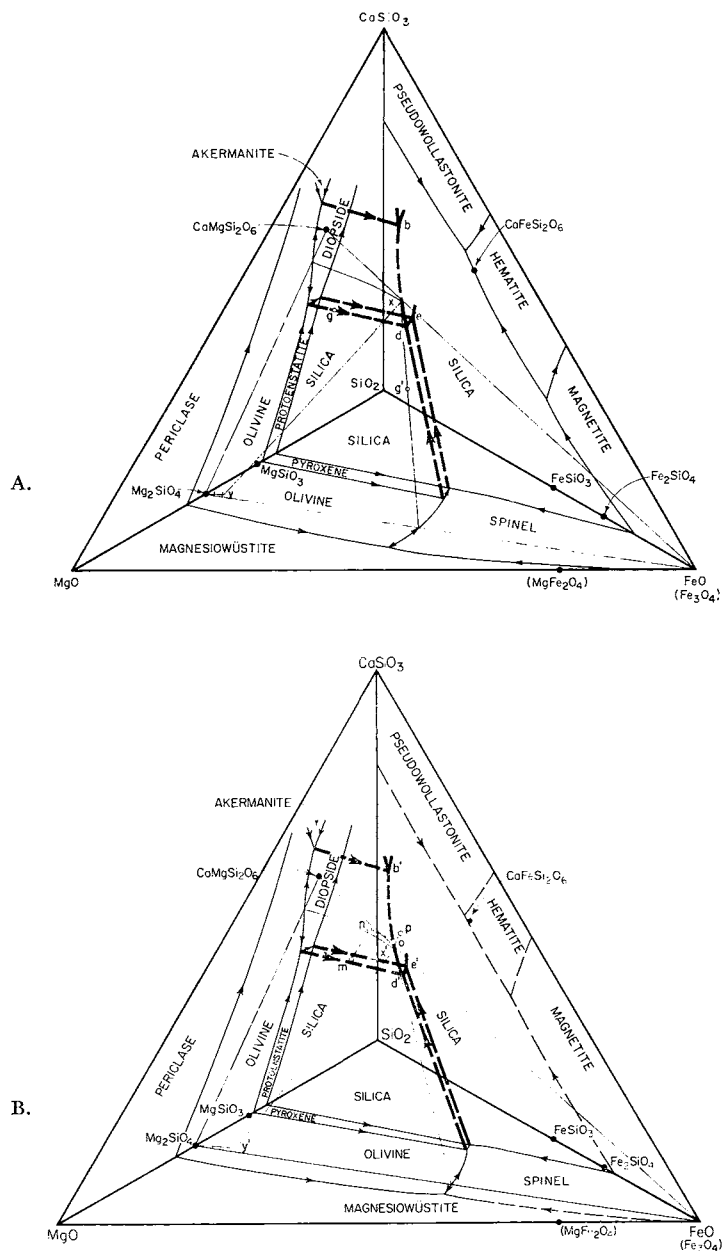
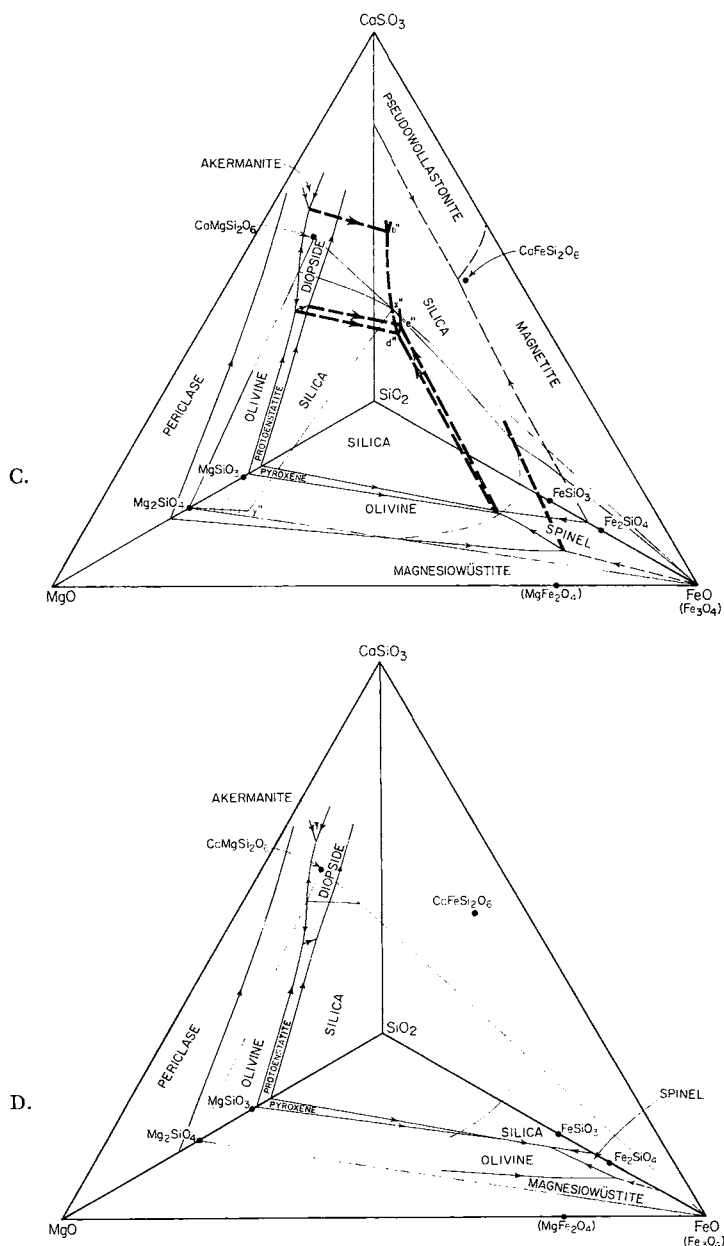


Fig. 6. The join CaSiO_3 - MgO -iron oxide- SiO_2 at $10^{-6.68}$ atm oxygen fugacity (A), at the oxygen fugacity produced by the equilibrium decomposition of pure CO_2 (B), at 10^{-6} atm oxygen fugacity (C), and at 10^{-8} atm oxygen fugacity (D). All diagrams are drawn in weight percent. Each tetrahedron is shown with the SiO_2 apex in the rear and the front face removed. Medium-weight lines in the faces of each tetrahedron are liquidus boundary curves, and heavy-weight dashed lines in the interior of each tetrahedron are univariant lines. Arrows indicate directions of decreasing temperature. The short and long dashed lines x - y , x' - y' , and x'' - y'' , are tie lines connecting the compositions of liquids x , x' , and x'' to olivines y , y' , and y'' (see table 2). The small amounts of calcium in these olivines are neglected. In each diagram, the gradu-



ations along the line from Mg_2SiO_4 to Fe_2SiO_4 are at intervals of 2 percent Fe_2SiO_4 . Compounds whose compositions have been projected onto the join MgO - FeO are shown in parentheses. Liquidus isotherms, the boundary curve between tridymite and cristobalite, and the region of immiscibility in the silica volume are omitted. The left face of each tetrahedron is after Kushiro (1964, fig. 28), Kushiro and Schairer (1963, fig. 25), and Osborn and Muan (1960), and the base is taken from figure 2. The right face of diagram A is after Phillips and Muan (1959, fig. 5), and the right face of diagrams B and C is inferred from the data of Bowen, Schairer, and Posnjak (1933b, fig. 6), Muan (1955, fig. 4), Phillips and Muan (1959, fig. 5), and Phillips and Muan (1960, fig. 5).

diopside-iron oxide mark the determined intersections of the plane of this join with divariant boundary surfaces in the tetrahedron.

It is useful at this point to consider the join diopside-iron oxide at $10^{-0.68}$ atm oxygen fugacity (fig. 3) and its relation to figure 6A. The fact that the line $t-u$ in figure 3 is not horizontal shows that liquids on the divariant surface $b-d-e$ (fig. 6A) are in equilibrium with spinel solid solutions rather than pure magnetite. The existence of point u in figure 3 demonstrates the existence of a univariant line in figure 6A along which diopside, spinel, hematite, and liquid are in equilibrium. This line is not shown in figure 6A because its location and relationship to the other univariant lines are not known.

Of particular significance is the series of experiments on the thirteenth mixture in appendix C. The composition of this mixture lies in the olivine primary phase volume and very near point x' on the univariant line $b'-d'$ (see figs. 4B and 6B). As shown in appendix C, this mixture consists of the equilibrium assemblage diopside, spinel, and liquid at 1297°C. The absence of olivine indicates that in the vicinity of point x' the univariant line $b'-d'$ must be a reaction line along which olivine dissolves while diopside and spinel crystallize during cooling at equilibrium. Further, it follows that line $b-d$ in figure 6A must also show this same reaction relation, for in this diagram the position of point x is nearly the same as point x' in figure 6B. At the same time, a liquid at point x must be in equilibrium with a diopside and a spinel that both contain less iron than the corresponding phases in equilibrium with a liquid at point x' in figure 6B. There are no data to indicate whether or not line $b''-d''$ in figure 6C shows this reaction relation.

At 10^{-8} atm oxygen fugacity (fig. 6D), the spinel volume is sufficiently reduced in size that it nowhere intersects the join forsterite-diopside-iron oxide. No univariant lines are drawn in this tetrahedron; none of these lines intersect the join forsterite-diopside-iron oxide, and their positions are therefore unknown.

FRACTIONAL CRYSTALLIZATION OF BASALTIC MAGMA

In order to determine to what extent the various igneous rocks in the Earth's crust are derived by fractional crystallization of basaltic magma, it is important to know experimentally the possible liquid compositions that can be derived by this process. This would require knowledge of a system of about nine or ten components. In the absence of this knowledge, petrologists have drawn preliminary conclusions based on data from three and four-component silicate systems and on relationships observed in the rocks themselves. One of the major points of controversy is the question of enrichment of residual liquids in iron oxides or in silica, soda, and potash (Bowen, 1928, 1954; Fenner, 1929; Wager and Deer, 1939; Kennedy, 1955; Osborn, 1959, 1962a). The present section deals with the relation between oxygen fugacity and the trend that is followed.

In discussing anhydrous, iron-bearing silicate systems, two types of crystallization paths have been distinguished, those at constant total composition and those at constant oxygen fugacity (Muan and Osborn, 1956, p. 136-138; Osborn, 1959, p. 611-630). In the former case, crystallization takes place without exchange of oxygen (or any other component) with the surroundings, and the oxygen fugacity at any temperature is determined by the equilibrium assemblage of liquid and crystalline phases. In the latter case, the crystallizing melt behaves as a system that is open with respect to oxygen but closed with respect to all other components. The oxygen fugacity is externally fixed and imposed on the melt. A variant of this latter case would be the situation in which the oxygen fugacity is imposed on the melt but varies continuously during cooling. This would occur, for example, if the melt were continuously equilibrated with a gas of constant H_2O/H_2 ratio.

Following Osborn (1959), crystallization of a melt without exchange of oxygen with the surroundings will be called crystallization at constant total composition. In an equilibrium situation in which the crystallizing melt is free to exchange oxygen with its surroundings and in which the oxygen fugacity is imposed by the surroundings on the melt, the oxygen fugacity of the melt will be referred to as buffered. This distinction works very well when discussing crystallization paths in anhydrous systems studied in the laboratory. However, in discussing the crystallization of magmas, the possible presence of water causes some slight complications; these complications will be taken up later in the section on magmas that contain water.

In this section, paths of fractional crystallization in the system $CaO-MgO-FeO-Fe_2O_3-SiO_2$ will be considered first with emphasis on comparisons with the simpler system, $MgO-FeO-Fe_2O_3-SiO_2$. The discussion of crystallization paths under conditions of buffered oxygen fugacity will be confined initially to the somewhat artificial situation of buffering at *constant* oxygen fugacity; this will be followed by a treatment of buffers whose oxygen fugacities vary with temperature. Then, in light of fractionation trends observed in these systems, some trends of chemical variation in volcanic rocks will be compared with the trend produced by fractional crystallization of the Skaergaard magma.

As with all silicate systems studied so far, the system $CaO-MgO-FeO-Fe_2O_3-SiO_2$ omits several important components found in igneous rocks, most notably some components necessary for the formation of feldspar; thus, enrichment trends in this system cannot be compared rigorously with enrichment trends in basaltic magma. Nevertheless, all of the major ferromagnesian minerals of basalts are included, so trends in this system are important as guide posts.

*Comparison of Fractional Crystallization in the Systems
 $CaO-MgO-FeO-Fe_2O_3-SiO_2$ and $MgO-FeO-Fe_2O_3-SiO_2$*

The following discussion is aimed toward an explanation of the following statements regarding paths of fractional crystallization of

haplobasaltic² compositions in the two systems, $\text{MgO-FeO-Fe}_2\text{O}_3\text{-SiO}_2$ and $\text{CaO-MgO-FeO-Fe}_2\text{O}_3\text{-SiO}_2$. These statements and the discussion that follows should be compared with the closely related discussions of Osborn (1959, 1962a, b), Osborn and Roeder (1960), and Roeder and Osborn (1966).

1. During the early stages of fractional crystallization, the starting composition exerts a strong control on the trend of enrichment of residual liquids. Enrichment in silica, in iron oxides, or in both can occur regardless of how the oxygen fugacity is controlled.

2. During the late stages of fractional crystallization, control of oxygen fugacity is important in determining the trend followed. Iron-enrichment is suppressed and silica-enrichment can be produced if the oxygen fugacity is buffered at a sufficiently high value that spinel has a large primary phase field or volume. On the other hand, iron-enrichment is produced either when crystallization takes place at constant total composition or when the oxygen fugacity is buffered at a sufficiently low value that the primary phase field or volume of spinel is either very small or absent.

3. At geologically reasonable oxygen fugacities, crystallization under conditions of buffered oxygen fugacity results in a greater suppression of iron-enrichment in the system $\text{CaO-MgO-FeO-Fe}_2\text{O}_3\text{-SiO}_2$ than in the system $\text{MgO-FeO-Fe}_2\text{O}_3\text{-SiO}_2$.

4. Buffering of the oxygen fugacity can suppress iron-enrichment regardless of whether the buffering agent causes the oxygen fugacity of the melt to increase, remain constant, or decrease during cooling. It is important only that the buffering agent be sufficiently oxidizing that a large field or volume of spinel occurs.

5. When crystallization takes place at constant total composition, the precipitation of spinel is accompanied by simultaneous enrichment of the residual liquid in iron. When the oxygen fugacity is buffered, iron-enrichment does not accompany the precipitation of spinel.

Early stages of fractional crystallization. — Figure 2A illustrates crystallization behavior in the system $\text{MgO-FeO-Fe}_2\text{O}_3\text{-SiO}_2$ when the oxygen fugacity is buffered at $10^{-0.68}$ atm. As explained earlier, this diagram can be treated as a ternary system for purposes of deducing crystallization paths. Point *n* is the haplobasaltic composition chosen by Osborn (1959, figs. 8 and 9) to show that silica-enriched residual liquids

² Bowen (1915, p. 161) used the word "haplobasaltic" to mean "simple basaltic". In the systems $\text{MgO-FeO-Fe}_2\text{O}_3\text{-SiO}_2$ and $\text{CaO-MgO-FeO-Fe}_2\text{O}_3\text{-SiO}_2$, haplobasaltic compositions are here taken to be those that (1) lie on or in the olivine, protoenstatite, or diopside field or volume, (2) contain silica in excess of that in the olivine join, and (3) contain less than 45 percent CaSiO_3 . For these compositions, the phase first precipitated on cooling is either olivine or a pyroxene, a situation in common with many basaltic liquids (for example, see Yoder and Tilley, 1962, figs. 27-30; Murata and Richter, 1966). Also, fractional crystallization of these compositions results in the precipitation of spinel, at least one pyroxene, and sometimes olivine; all of these phases characteristically precipitate from basaltic liquids. Some of the compositions included might be regarded as more ultramafic than basaltic, but a more complicated definition designed to eliminate the ultramafic compositions would not alter the conclusions reached below.

can result from fractional crystallization at constant oxygen fugacity. During the initial stages of cooling, the liquid composition is enriched in silica as it moves along the boundary curve $n-c$. Point n' also could be considered a reasonable haplobasaltic composition. On cooling of this mixture, the liquid becomes enriched initially in iron oxides and depleted in silica as it moves through the pyroxene field toward m . Thus, when the oxygen fugacity is buffered, the starting composition exerts a strong control on the initial trend that is followed.

Figure 6A shows crystallization paths in the system $\text{CaO-MgO-FeO-Fe}_2\text{O}_3\text{-SiO}_2$ when the oxygen fugacity is buffered at $10^{-0.68}$ atm. On cooling of a composition at point g , protoenstatite and diopside precipitate as the liquid fraction moves toward the vicinity of invariant point e . The liquid is thus enriched in iron oxides. Point g' lies on the divariant surface between olivine and spinel. On cooling of this mixture, olivine and spinel precipitate as the liquid fraction moves along the divariant surface toward invariant point d . In this case, the liquid is enriched in silica. Again, both early silica-enrichment and early iron-enrichment are possible when the oxygen fugacity is buffered.

Early enrichment trends that occur in the system $\text{MgO-FeO-Fe}_2\text{O}_3\text{-SiO}_2$ when crystallization takes place at constant total composition can be deduced from figure 7. Point r lies in the olivine volume, and on precipitation of olivine during cooling the liquid fraction is enriched predominantly in silica but also in iron oxides as it moves through the olivine volume along the curved path $r-s$. The liquid fraction derived from crystallization of mixture r' is enriched in iron oxides and depleted in silica as it moves toward the peritectic point g . Again, the starting composition greatly influences the initial enrichment trend, but in this case crystallization has taken place at constant total composition.

In general, then, the early trend toward silica or toward iron is strongly controlled by the starting composition; either trend can occur regardless of whether the oxygen fugacity is buffered or the total composition remains constant. Pending more precise knowledge of which

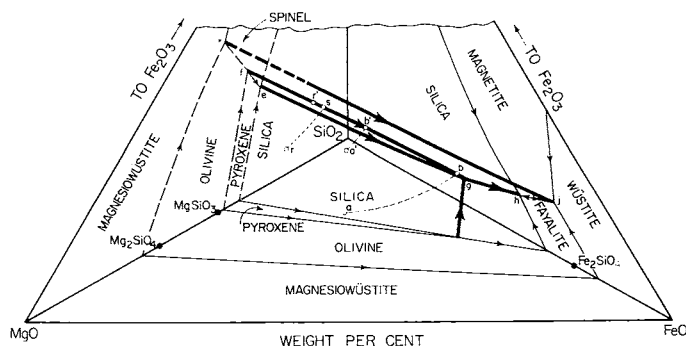


Fig. 7. A portion of the system $\text{MgO-FeO-Fe}_2\text{O}_3\text{-SiO}_2$ (after Muir and Osborn, 1956, fig. 12) to illustrate paths of fractional crystallization.

starting compositions are most analogous to basalts, it is concluded that the trend of enrichment that occurs in the early stages of fractional crystallization of basaltic magma need not necessarily be related to the manner in which the oxygen fugacity is controlled.

Suppression of iron-enrichment during the late stages of fractional crystallization.—During the late stages of fractional crystallization of haplo-basaltic mixtures, the effect of buffering the oxygen fugacity assumes greater importance in determining the path of the liquid. It can be seen in figure 2A that regardless of the early trend of the liquid, continuous iron-enrichment is not possible when the oxygen fugacity is buffered at $10^{-0.68}$ atm (also see Osborn, 1959, p. 627-628). Thus, in the case of mixture *n'*, it was observed earlier that the liquid initially becomes enriched in iron; however, it turns abruptly toward the invariant point *d* when it reaches the field of spinel at *m*. In a similar way, the spinel volume in figure 6A suppresses iron-enrichment. Haplo-basaltic mixtures, such as *g*, lying to the left of the spinel volume will, on cooling, yield residual liquids that are enriched in iron until they reach the surface of the spinel volume. As soon as spinel starts to precipitate, iron-enrichment stops and silica-enrichment is produced (also see Osborn, 1962a, p. 219). Thus, when the oxygen fugacity is buffered, iron-enrichment is arrested during the late stages of crystallization, regardless of the initial trend of the liquid.

As we shall now see, one could conclude from the system $MgO-FeO-Fe_2O_3-SiO_2$ that the oxygen fugacity required to suppress iron-enrichment in residual liquids is too high for buffering of oxygen fugacity to be important in controlling differentiation trends of basaltic magma. In figure 2, the size of the spinel field gradually shrinks as oxygen fugacity decreases. As pointed out by Roeder (ms), this produces a gradual change in the extent to which liquid compositions can move to the right and become enriched in iron oxides during fractional crystallization at constant oxygen fugacity. Thus, at $10^{-0.68}$ atm oxygen fugacity (fig. 2A) the spinel field is large, and liquid crystallization paths are prevented from continuing toward the iron oxide apex. However, with fractional crystallization at an oxygen fugacity of 10^{-6} atm or lower (figs. 2C and 2D), the spinel field is small, and liquid crystallization paths continue toward relatively iron-enriched compositions without turning noticeably toward the silica apex. Fudali (1965) determined experimentally that the oxygen fugacities in equilibrium with nine andesites and basalts at $1200^\circ C$ are in the range of $10^{-6.4}$ to $10^{-8.5}$ atm. These rocks thus crystallized in a range of oxygen fugacity too low for significant suppression of iron-enrichment as indicated in the system $MgO-FeO-Fe_2O_3-SiO_2$.

Addition of CaO to the system dissipates this difficulty to the buffer concept, for even though the spinel field on the base of each tetrahedron (fig. 6) shrinks gradually as oxygen fugacity is reduced, the spinel volume in the interior of each tetrahedron contracts very little

as the oxygen fugacity is decreased from $10^{-0.68}$ to 10^{-6} atm. This can be seen in figures 6A to C, in which the positions of points x , x' , and x'' are almost coincident. Thus, at 10^{-6} atm oxygen fugacity (fig. 6C), starting compositions containing CaO produce residual liquids enriched in iron approximately the same amount as if the oxygen fugacity were maintained at $10^{-0.68}$ atm (fig. 6A). This fact completely negates the idea that geologically reasonable oxygen fugacities are too low for the suppression of iron-enrichment through buffering. The presence of CaO simultaneously makes the laboratory compositions more realistic geologically and reduces the oxygen fugacity required for the suppression of iron-enrichment.

Iron-enrichment during the late stages of fractional crystallization.—Iron-enrichment is enhanced either when the total composition remains constant or when the oxygen fugacity is buffered at a sufficiently low value that the spinel field or volume is very small or absent. Crystallization at constant total composition in the system $\text{MgO-FeO-Fe}_2\text{O}_3\text{-SiO}_2$ has been discussed previously (Osborn, 1959, p. 618-619; Muan and Osborn, 1956, p. 136-137). Unfortunately, the present data are insufficient for an understanding of crystallization paths in the system $\text{CaO-MgO-FeO-Fe}_2\text{O}_3\text{-SiO}_2$ when the total composition remains constant.

The enhancement of iron-enrichment that occurs when the oxygen fugacity is buffered at a low value can be seen in figure 2D. In this diagram, the spinel field is very small; fractional crystallization of haplobasaltic mixtures lying in the olivine or pyroxene primary phase field therefore yields a final iron-enriched liquid at the invariant point at which the olivine, pyroxene, and spinel fields meet.

The spinel volume in the system $\text{CaO-MgO-FeO-Fe}_2\text{O}_3\text{-SiO}_2$ at 10^{-8} atm oxygen fugacity is also small (fig. 6D), for even though the positions of the univariant lines in the tetrahedron are not known, the extent of the spinel volume must be more restricted than at higher oxygen fugacities since it nowhere intersects the join $\text{Mg}_2\text{SiO}_4\text{-CaMgSi}_2\text{O}_6\text{-iron oxide}$. The spinel volume must entirely disappear at some lower oxygen fugacity, as inferred by Osborn (1962a, fig. 3). Thus, when the oxygen fugacity is buffered at a low value (at least less than 10^{-8} atm), haplobasaltic liquids are free to move toward compositions greatly enriched in iron oxides.

Buffering under conditions other than constant oxygen fugacity.—One might contend that the above discussion of crystallization paths at constant oxygen fugacity cannot apply to basaltic magma since the oxygen fugacity in equilibrium with a cooling magma would rarely remain approximately constant even if buffering occurred. For example, suppose a fluid in the rock adjacent to a magma buffers the oxygen fugacity of the magma and is present in sufficient excess that any buffering action would produce a negligible change in the composition of the fluid. For simplicity, let this buffering fluid consist of an equilibrium gas mixture of H_2O , H_2 , and O_2 . In order for the gas to impose a constant oxygen

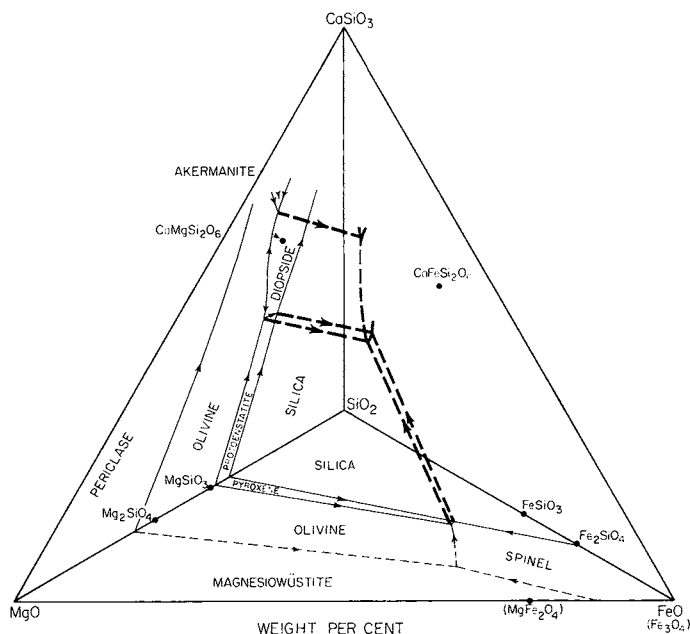


Fig. 8. The join CaSiO_3 - MgO -iron oxide- SiO_2 at the oxygen fugacity produced by a gas of constant ratio CO_2/H_2 of 132. All symbols have the same meanings as those in figure 6. The base of the tetrahedron is after Muan and Osborn (1956, fig. 7), and the left face is after Kushi (1964, fig. 28), Kushi and Schairer (1963, fig. 25), and Osborn and Muan (1960).

fugacity on the magma, the ratio $\text{H}_2\text{O}/\text{H}_2$ in the gas would have to increase continuously as the magma cooled (see Muan and Osborn, 1965, fig. 15). It would be very fortuitous if the ratio $\text{H}_2\text{O}/\text{H}_2$ were to change by just the right amount required to maintain the oxygen fugacity approximately constant at all temperatures. A more realistic assumption might be to let the bulk composition of the buffering gas remain constant. In this case the oxygen fugacity would continuously decrease on cooling, and one might suppose that the fractionation trends discussed above at constant oxygen fugacity would then be greatly altered. As will now be shown, some changes occur, but the changes are not large enough to alter any of the conclusions.

Trends of fractional crystallization to be expected when the system is buffered by a gas of constant bulk composition can be deduced from figures 6B and 8. In figure 6B the buffering gas is pure CO_2 plus equilibrium amounts of CO and O_2 formed by decomposition of the CO_2 . This buffer yields an equilibrium diagram nearly identical to one that would result from a buffer of pure water plus its decomposition products H_2 and O_2 , for the variation of oxygen fugacity with temperature for pure CO_2 is very close to that for pure H_2O (see fig. 9). The similarity of the equilibrium relations to those at $10^{-0.68}$ atm oxygen fugacity (fig.

6A) shows that fractional crystallization with pure CO_2 or pure H_2O as a buffer yields enrichment trends very similar to those that occur during crystallization at constant oxygen fugacity. This occurs despite the fact that the oxygen fugacity decreases with falling temperature (see fig. 9).

Inferred equilibrium relationships at a constant ratio CO_2/H_2 of 132 are illustrated in figure 8. In this case the oxygen fugacity is buffered by a gas of constant bulk composition that consists of CO_2 and H_2 in the ratio of 132 at room temperature. At high temperature these two gases react to form an equilibrium assemblage of H_2O , H_2 , CO_2 , CO , and O_2 . The equilibrium oxygen fugacity of the gas buffer $\text{CO}_2/\text{H}_2 = 132$ decreases much more rapidly with falling temperature than that of pure CO_2 (see fig. 9), but despite this more rapid decrease, the equilibrium relationships are still very similar to those at constant oxygen fugacity shown in figures 6A and 6C.

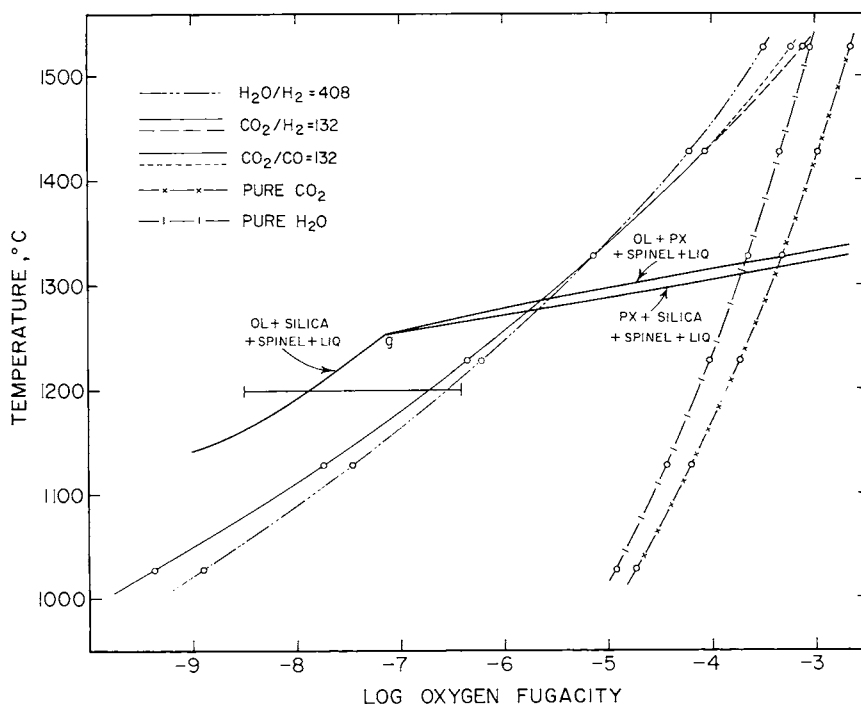


Fig. 9. Equilibrium oxygen fugacities produced by gases of various compositions at a total pressure of 1 atm. Gas mixtures are expressed in mole ratios. Open circles are points calculated from the tabulations given by Coughlin (1954, tables 27, 28, and 56). The horizontal line at 1200°C shows the range of oxygen fugacities in equilibrium with various basalts and andesites determined by Fudali (1965, table 3). The heavy solid lines show the variation of oxygen fugacity with temperature along three liquidus univariant lines in the system $\text{MgO-FeO-Fe}_3\text{O}_4\text{-SiO}_2$ (see fig. 7, data from Muan and Osborn, 1956). A fourth univariant line extending from point *g* is omitted. PX = pyroxene, OL = olivine, LIQ = liquid.

If a gas buffer of a constant $\text{H}_2\text{O}/\text{H}_2$ or CO_2/CO ratio had been chosen, then ratios of 408 and 132 respectively would yield equilibrium diagrams almost identical to figure 8. This is because the variation of oxygen fugacity with temperature for these buffers is only slightly different than for a buffer of constant CO_2/H_2 ratio of 132 (see fig. 9).

For all these buffers of constant gas composition, the oxygen fugacity decreases with cooling but not sufficiently to allow residual liquids to become enriched in iron oxides. Such buffers thus produce an effect similar to a gas buffer of constant high oxygen fugacity. If a less oxidizing buffer had been chosen, such as a gas with a CO_2/H_2 ratio of 19, then the olivine, protoenstatite, and diopside volumes in figure 8 would be extended to the right at the expense of the spinel volume (see also Muan and Osborn, 1956, fig. 10). Liquids moving to the right during fractional crystallization would not turn toward the silica apex but would continue to become enriched in iron oxides. The effect would be similar to that produced by a gas buffer of constant low oxygen fugacity. In both cases, the continued trend toward enrichment in iron oxides is caused by a small spinel volume, and spinel would precipitate only during the final stages of crystallization if at all.

It is interesting to compare the variation of oxygen fugacity with temperature that occurs during buffering with some variations that occur when the total composition remains constant. For crystallization at constant composition in the system $\text{MgO}-\text{FeO}-\text{Fe}_2\text{O}_3-\text{SiO}_2$ (fig. 7), fractional crystallization paths of most haplobasaltic compositions eventually intersect one of the univariant lines $f-g$ or $e-g$. After intersecting one of these lines, crystallization paths continue to the right toward point g either along one of the two univariant lines or on the divariant surface $e-f-g$. The oxygen fugacity along these lines (fig. 9) decreases more rapidly with temperature than the oxygen fugacity in equilibrium with any of the gas buffers. Thus, for crystallization paths that have reached one of the two univariant lines $f-g$ or $e-g$, further cooling under conditions of buffered oxygen fugacity results in oxidation of the melt even though the oxygen fugacity imposed by the buffer decreases with temperature.

Magma that contain water.—All of the discussion so far has concerned the crystallization of anhydrous melts. In order for buffering to occur, such melts must behave as systems open to oxygen. However, for a crystallizing magma containing water in a separate vapor phase (saturated with water), the oxygen fugacity might be buffered by a fluid in the surrounding rock solely by diffusion of hydrogen across the boundaries of the magma, a process analogous to the technique for buffering the oxygen fugacity of hydrothermal equilibrium experiments in the laboratory (Eugster, 1957; see also discussions by Eugster, 1959, p. 424; Chinner, 1960, p. 212; and Osborn, 1959, p. 643-644). In the case of oxidation of the magma by this mechanism, the source of oxygen would be the contained water, and the hydrogen produced by

decomposition of the water would diffuse out of the magma into the adjacent rock. Water in the amount of only 1.25 weight percent in a basaltic magma containing 10 weight percent FeO could provide sufficient oxygen for complete oxidation of this FeO to Fe_2O_3 . In nature there could be all gradations between crystallization at constant total composition and crystallization with buffered oxygen fugacity. Diffusion of hydrogen might occur but not with sufficient speed to establish a state of buffering at equilibrium with a fluid in the surrounding rock. In this case, the oxidation state of the magma would be altered but not as strongly as if buffering at equilibrium had occurred.

Now consider a hydrous magma that again contains water in a separate vapor phase but crystallizes as a closed system. During cooling and crystallization, the oxygen fugacity would again fall at a rate intermediate between that for crystallization of an anhydrous melt at constant total composition and that of an anhydrous melt buffered by a gas of constant composition. Similarly, the trend of enrichment would be of an intermediate type. This is because the water would provide a limited reservoir for exchange of oxygen with the melt. The trend of enrichment would depend on the amount of water in the magma and the $\text{H}_2\text{O}/\text{H}_2$ ratio in the vapor at the start of crystallization. A magma containing only trace amounts of water would differentiate in nearly the same way as an anhydrous magma crystallizing at constant total composition, but for a magma saturated with water, the relative proportions of H_2O and H_2 in the vapor at the start of crystallization would be important. If the ratio $\text{H}_2\text{O}/\text{H}_2$ were low, say less than 20, then iron-enrichment would occur. If this ratio were high, say about 400, iron-enrichment would be suppressed but not as strongly as if the magma were buffered by a large external reservoir containing H_2O and H_2 in the ratio of 400:1. During cooling, the ratio $\text{H}_2\text{O}/\text{H}_2$ in the vapor would decrease, and the oxygen content of the remainder of the magma would increase.

Thus, a complete range of enrichment trends could occur due either to imperfect establishment of equilibrium between an external buffer and the magma or to crystallization of a water-rich and hydrogen-poor magma as a closed system.

In view of the fact that a hydrous magma crystallizing as a closed system could be oxidized by the contained water, the total composition of a hydrous melt will refer only to the anhydrous portion. Thus, crystallization of a hydrous magma as a closed system will *not* be taken to mean crystallization at constant total composition.

Iron-enrichment and the precipitation of spinel.—It has long been recognized that precipitation of magnetite from a fractionally crystallizing basaltic magma is entirely compatible with simultaneous iron-enrichment of the residual liquid (Wager and Deer, 1939, p. 220). On the other hand, some sequences of volcanic rocks whose chemical variations have been attributed to fractional crystallization show precipitation of

magnetite accompanied by a decrease in the amount of total iron oxides in the liquid (for example, see Carmichael, 1964).

In view of these contrasting relationships, it is interesting to note that for haplobasaltic compositions in the system $\text{MgO-FeO-Fe}_2\text{O}_3\text{-SiO}_2$, *if crystallization occurs at constant total composition, the precipitation of spinel is accompanied by enrichment of the liquid fraction in iron.* On the other hand, *if the oxygen fugacity is buffered during crystallization, precipitation of spinel is not accompanied by enrichment of the liquid fraction in iron.*

A brief look at some of the equilibrium diagrams will verify the above generalizations regarding the precipitation of spinel. In figure 7, the precipitation of spinel occurs when a liquid lying on the surface *e-g-h-j-k-f* is cooled. If crystallization takes place at constant total composition, the liquid composition will move along this surface toward compositions richer in iron. On the other hand, when the oxygen fugacity is buffered at $10^{-0.68}$ atm (fig. 2A), the precipitation of spinel along the boundary curve *n-c-d* is accompanied not by iron-enrichment but by silica-enrichment. Finally, in figure 2D, extensive iron-enrichment can occur since the oxygen fugacity is buffered at a low value. However, spinel precipitates only as the last residual liquid crystallizes, not during the time when haplobasaltic liquids are becoming enriched in iron. Similarly, if the buffering agent is a gas of constant composition with a low ratio CO_2/H_2 of 24, iron-enrichment occurs, but spinel precipitates only as the last residual liquid crystallizes (see Muan and Osborn, 1956, fig. 9). Thus, when iron-enrichment occurs and the oxygen fugacity is buffered either at constant oxygen fugacity or by a gas of constant composition, the precipitation of spinel is not accompanied by enrichment of the liquid fraction in iron.

When the total composition of haplobasaltic compositions in the system $\text{MgO-FeO-Fe}_2\text{O}_3\text{-SiO}_2$ remains constant, a higher proportion of Fe_2O_3 causes earlier precipitation of spinel, but the trend toward iron-enrichment always remains after the appearance of spinel as a crystallizing phase. This fact is illustrated by the crystallization paths of points *a* and *a'* in figure 7. Point *a*, lying on the divariant surface between the olivine and pyroxene volumes, is very low in Fe_2O_3 . On fractional crystallization, the liquid composition travels along the line *a-b* in the divariant surface as olivine and pyroxene precipitate.³ Spinel starts to precipitate at *b* only after extensive iron-enrichment has occurred. Further cooling causes continued iron-enrichment as the liquid composition moves from *b* through the invariant point *g* to *h*. On the other hand, point *a'*, which also lies on the divariant surface between olivine and pyroxene, is relatively richer in Fe_2O_3 . Fractional crystallization of this composition causes the composition of the liquid fraction to

³ For simplicity of discussion, the divariant surface between the olivine and pyroxene volumes and the univariant line *f-g* are assumed not to show a reaction relation in the region discussed. Removal of this assumption would not affect the conclusions.

move along the path $a'-b'$. At b' spinel starts to precipitate before extensive iron-enrichment has occurred; it continues to do so as the composition of the liquid moves to the invariant point g and then to h .

Insofar as the data extend, the addition of CaO to the system $\text{MgO-FeO-Fe}_2\text{O}_3\text{-SiO}_2$ does not change the relationships just discussed. Thus, when the oxygen fugacity is buffered at any value between $10^{-0.68}$ and 10^{-6} atm (figs. 6A-C), the precipitation of spinel is never accompanied by enrichment of the liquid fraction in iron. Buffering the oxygen fugacity at values less than 10^{-8} atm would produce iron-enrichment, but the spinel volume would be small, and spinel would precipitate only during the final stages of fractional crystallization, if at all.

In studying rock sequences, it would be useful to be able to note the precipitation of spinel and the trend of enrichment and thereby infer whether or not the oxygen fugacity was buffered during crystallization. This would require that the italicized statements in the second paragraph of this section remain valid after transposition of the conditions and conclusions. Unfortunately, the statements are then no longer rigorously true due to the possibility of transitional conditions between constant total composition and buffered oxygen fugacity. Nevertheless, it is still possible to use the precipitation of spinel and iron-enrichment as a rough indicator of crystallization at constant or nearly constant total composition. Similarly, the precipitation of spinel without iron-enrichment may be used as a rough indicator that the oxygen fugacity was buffered.

It is possible that the addition of other components to the systems considered here would invalidate the above discussion regarding the precipitation of spinel and the trend of enrichment. This can be settled finally only by the study of systems containing all the components of basaltic magma, but the equilibrium diagrams of Roeder and Osborn (1966), which indicate the effects of the addition of Al_2O_3 , only further confirm the generalizations stated here.

The above discussion of buffering is pertinent to the crystallization of magmas only if buffering of oxygen fugacity occurs in nature. In this regard, it is significant that Buddington and Lindsley (1964) found evidence that iron-titanium spinels initially crystallized at high temperatures frequently have been oxidized upon subsequent cooling. They showed that in many cases, buffering of the oxygen fugacity of the rock by a gas of constant composition is sufficient to produce the observed oxidation. If buffering of rocks occurs during cooling subsequent to crystallization, then buffering of a magma during crystallization must be considered a likely process.

The main conclusions of this section are that buffering of oxygen fugacity is capable of significantly altering the liquid crystallization paths of compositions similar to basalts, that basalts crystallize in a range of oxygen fugacity where buffering is important, and that buffering of the oxygen fugacity of a magma is a reasonable geologic process.

Even though the types of buffering conditions discussed above are idealized and simplified, the results produced point toward the effects to be expected from buffering of the oxygen fugacity of basaltic magma.

*Trends of Chemical Variation of the Skaergaard Magma
and of Volcanic Rocks*

The Skaergaard intrusion is one of the most extensively documented examples of a series of rocks whose chemical variations are known to be the result of extreme fractional crystallization of basaltic magma (Wager and Deer, 1939; Taylor and Epstein, 1963). The exposed rocks are those formed during the middle and late stages of fractional crystallization. As explained earlier, it is the late stages of crystallization that are closely related to the way in which oxygen fugacity is controlled. This intrusion therefore offers a good opportunity for a comparison between a known example of fractional crystallization of basaltic magma and fractionation trends deduced from the equilibrium diagrams under varying conditions of oxygen fugacity. The discussion here will focus on two features of the Skaergaard intrusion. One is the unusually high enrichment in $\text{FeO} + \text{Fe}_2\text{O}_3$ achieved by the late liquid fraction. As shown in figure 10, the Skaergaard magma achieved a maximum concentration of $\text{FeO} + \text{Fe}_2\text{O}_3$ of about 22 percent; a concentration of even 16 percent $\text{FeO} + \text{Fe}_2\text{O}_3$ is unusual in igneous rocks. The other feature is the time of appearance of magnetite as a precipitating phase (see fig. 10).

Osborn (1959, p. 634) attributed the extreme iron-enrichment of the Skaergaard magma to crystallization at constant total composition. When this condition is imposed in the equilibrium diagrams, spinel must always precipitate at some point in the history of fractional crystallization. Later, Osborn (1962a, p. 225) suggested that the Skaergaard trend was due to crystallization at low oxygen fugacity without the precipitation of spinel, a situation in which the oxygen fugacity must be buffered at a low value. According to Wager (1960), magnetite first precipitated from the Skaergaard magma long before iron-enrichment ceased (see fig. 10), and it continued to precipitate throughout the formation of the remaining layered series. This indicates that the Skaergaard magma crystallized at constant total composition in accordance with the first suggestion of Osborn, for in the equilibrium diagrams discussed above, the precipitation of spinel with simultaneous iron-enrichment indicates crystallization at constant total composition. This conclusion fits well with the fact that the Skaergaard magma apparently contained very little water (Kennedy, 1955, p. 496; Taylor and Epstein, 1963, p. 55, 65-68). In a dry magma there would be no adequate source of oxygen for oxidation of the magma.

It is not intended that these conclusions regarding the Skaergaard intrusion necessarily should be applied to every layered intrusion or differentiated sill that shows iron-enrichment. As shown earlier, initial iron-enrichment may be expected for certain compositions regardless of

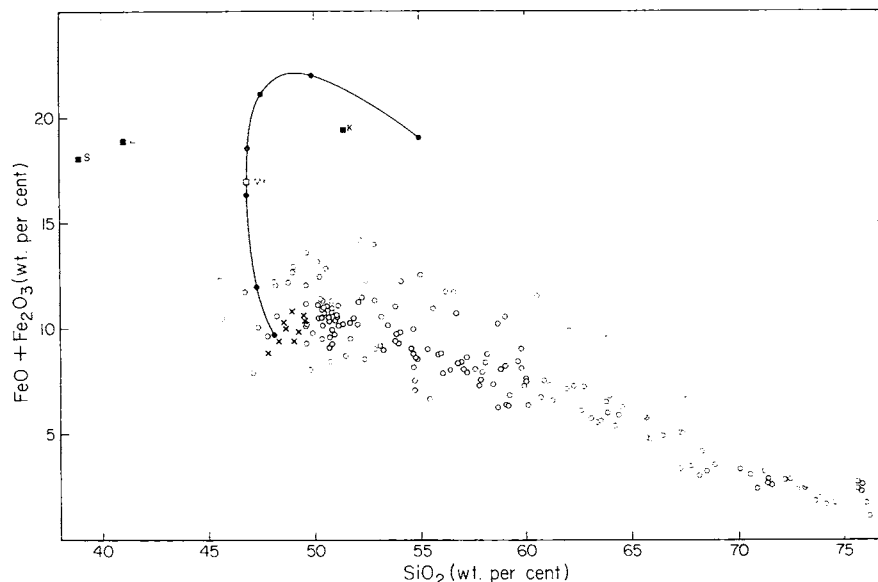


Fig. 10. Chemical variation of the Skaergaard magma and selected volcanic rocks. Filled circles show calculated compositions of the Skaergaard magma at successive stages of differentiation, as given by Wager (1960, table 4). The open square labeled Mt shows the point at which magnetite first started to precipitate from the Skaergaard magma (after Wager, 1960). Crosses show compositions of lavas given in table 5. Open circles show compositions of lavas from six areas of volcanic activity. The analyses are distributed as follows: 135 from the Fuji-Hakone-Izu area, Japan; 26 from the Medicine Lake Highland, California; 6 from the Galapagos Islands; 6 from Rishiri volcano, Japan; 5 from Funagata volcano, Japan; and 3 from the Iki Islands, Japan. Analyses from the Fuji-Hakone-Izu area are from Asayama (1953), Hirokawa and Suyama (1955), Katsura (1956), Kawano (1950), Kuno (1933, 1935, 1936a, 1936b, 1950a, 1954, 1960, 1962), Nagashima (1953), and Tsuya (1929, 1935, 1937, 1942, 1955); those from the Medicine Lake Highland are taken from Andersen (1933, 1941), Powers (1932), and Yoder and Tilley (1962, p. 362); those from the Galapagos Islands are due to Lacroix (1927), Richardson (1933), and Washington and Keyes (1927); those from Funagata volcano are taken from Kawano, Yagi, and Aoki (1961); those from the Iki Islands are due to Aoki (1959); and those from Rishiri volcano are from Katsui (1953). From the Iki Islands, only analyses of the Miocene (?) flows were used because analysis 7 in table 3 is of a flow extruded during this period of volcanism. According to the usage of Chayes (1964, p. 1581), all the rocks whose analyses are identified by crosses are subalkaline. Their associated lavas are also subalkaline except for one analysis of an alkaline lava from the Medicine Lake Highland, two such analyses from the Galapagos Islands, and three from Rishiro volcano. Point K is a segregation vein in a lava from Ō-sima Island, Japan (Kuno, 1965, p. 304), point L is a lava from Madagascar (Lacroix, 1923, p. 57), and point S is a lava from Southern Rhodesia (Swift and others, 1953, p. 40).

the control of oxygen fugacity, and this iron-enrichment could continue if the oxygen fugacity were buffered at a low value. Each example of iron-enrichment must be considered separately.

Apparently, lavas similar in composition to the late, extremely iron-enriched Skaergaard liquids are nonexistent or nearly so; an examination of over 8000 analyses of lavas failed to uncover such compositions.

As stated earlier, the maximum iron-enrichment reached by the Skaergaard magma is about 22 percent $\text{FeO} + \text{Fe}_2\text{O}_3$, but only two complete analyses of fresh lavas were found that contain more than 18 percent $\text{FeO} + \text{Fe}_2\text{O}_3$ (see fig. 10). Neither contains more than 41 percent SiO_2 , and they are therefore of doubtful similarity to the later Skaergaard liquids which contain more than 46.8 percent SiO_2 . In any case, lavas as enriched in $\text{FeO} + \text{Fe}_2\text{O}_3$ as the Skaergaard magma are extremely rare. Kuno (1965, p. 304) gave an analysis of a segregation vein (see fig. 10) that has many compositional similarities to the iron-enriched Skaergaard liquids, but the analysis was not representative of a large volume of lava of this composition. If the previous conclusion is accepted that the Skaergaard magma crystallized at constant total composition and if magmas similar in composition to the initial Skaergaard magma have commonly moved into the Earth's crust to regions of moderate or low pressure,⁴ then it must be that only rarely, if ever, have these magmas produced lavas whose compositions are controlled by extreme fractional crystallization at constant total composition. If lavas of varying compositions were produced from these magmas primarily by strong fractional crystallization, the oxygen fugacities of these magmas must have been controlled by oxidizing buffers.

It might be supposed that the differentiation trend of the Skaergaard magma is due to an unusual starting composition and that the extreme rarity of a similar degree of iron-enrichment in volcanic rocks is due to the rarity of this starting composition. Quite the contrary, recent data (Engel and Engel, 1964; Engel, Engel, and Havens, 1965; Nicholls, Nalwalk, and Hays, 1964) indicate that lavas close to the composition of the initial Skaergaard magma very commonly if not characteristically occur in the deeper parts of the oceans. An average of ten analyses of lavas from the ocean floors is shown in table 3 for comparison with the composition of the initial Skaergaard magma. If these abundant lavas represent magma compositions that have fractionally crystallized at constant total composition, lavas similar in composition to the later Skaergaard liquids should exist. No such lavas have been reported in the literature.

Additional evidence comes from an examination of lavas close in composition to the initial Skaergaard magma that are associated in time and place with other lavas of different compositions. Table 3 shows nine analyses of lavas similar to the Skaergaard initial magma taken from six areas of volcanic activity. All available analyses of their associated lavas (fig. 10) show no compositions close to the amount of $\text{FeO} + \text{Fe}_2\text{O}_3$ that existed in the later Skaergaard liquids. Therefore, the nine lavas similar in composition to the Skaergaard magma cannot be related to their associated lavas solely through fractional crystal-

⁴As mentioned earlier, the discussion here is not concerned with fractional crystallization in the upper mantle where high pressure phases appearing at the liquidus surface would alter the fractionation trends.

TABLE 3

Analyses of lavas close in composition to the Skaergaard initial magma

	1	2	3	4	5	6	7	8	9	10	11
SiO ₂	48.08	49.34	48.27	47.77	48.98	48.65	48.96	49.26	49.56	48.57	49.51
Al ₂ O ₃	17.22	17.04	18.28	18.52	18.92	17.50	17.47	17.71	17.88	19.25	18.19
Fe ₂ O ₃	1.32	1.99	1.04	1.49	2.22	0.25	2.27	2.67	2.82	2.56	2.89
FeO	8.44	6.82	8.31	7.31	7.12	9.75	8.54	7.12	7.54	7.70	7.66
MnO	0.16	0.17	0.17	0.14	0.09	0.25	0.17	0.05	0.16	0.15	0.28
MgO	8.62	7.19	8.96	9.88	7.42	6.61	6.72	7.91	7.03	6.38	7.07
CaO	11.38	11.72	11.32	11.32	10.04	11.85	11.03	10.01	10.92	11.21	9.83
Na ₂ O	2.37	2.73	2.80	2.55	3.04	2.15	2.12	3.08	1.50	1.73	2.49
K ₂ O	0.25	0.16	0.14	0.12	0.44	0.38	0.32	0.56	0.22	0.16	0.48
TiO ₂	1.17	1.49	0.89	0.71	1.16	2.10	0.72	1.25	0.72	0.75	0.64
P ₂ O ₅	0.10	0.16	0.07	0.07	0.14	0.21	0.14	0.19	0.06	0.10	0.17
H ₂ O ⁺	1.01*	0.69	0.15	0.31	0.34	tr.	0.90	0.36	1.16	0.74	0.45
H ₂ O ⁻	0.05	0.58	0.07	0.11	0.05	0.10	0.66	0.17	0.86	0.85	0.27
Total	100.17	100.08	99.81	100.30	99.96	99.80	100.02	100.34	100.43	100.15	99.93

1. Skaergaard initial magma (Wager, 1960, p. 375).
2. Average of 10 analyses of lavas from the Atlantic and Pacific Ocean floors (Engel, Engel, and Havens, 1965, p. 721).
3. and 4. Basalts from Warner Flow, Medicine Lake Highland, California (Yoder and Tilley, 1962, p. 362).
5. Modoc basalt, Medicine Lake Highland, California (Anderson, 1941, p. 387).
6. Basalt from Narborough Island, Galapagos Islands (Richardson, 1933, p. 52).
7. Basalt from Iki Island, Japan (Aoki, 1959, table 15).
8. Basalt from Rishiri Island, Hokkaido, Japan (Katsui, 1953, p. 249).
9. Basalt from Funagata volcano, near Sendai, Japan (Kawano, Yagi, and Aoki, 1961, p. 25).
10. Basalt from northeastern Izu, Japan (Tsuya, 1937, p. 239).
11. Basalt from Maruno-yama volcano on the northern flank of Amagi volcano, eastern central Izu, Japan (Tsuya, 1937, p. 257).

* Considered by Wager (1960, table 2) to be high due to alteration of olivine.

lization at constant total composition. The extent to which other processes such as contamination may have participated in the production of the chemical variations in these volcanic rocks must remain undetermined for the present, but *if* fractional crystallization at moderate or low pressure was the controlling factor, the oxygen fugacity in each case must have been controlled by an oxidizing buffer.

THE REACTION OF OLIVINE AND LIQUID TO FORM PYROXENE AND SPINEL

Several examples of reaction rims on olivine consisting of both magnetite and hypersthene have been reported (Kuno, 1950b, p. 970; Muir, Tilley, and Scoon, 1957, fig. 4; Snyder, 1959, p. 192; Yoder and Tilley, 1962, p. 425). Kuno (1950b) suggested that these compound reaction rims were due to a frozen, partially completed reaction of olivine with the enclosing liquid to form hypersthene and magnetite, but Yoder and Tilley (1962, p. 425) attributed such rims to oxidation of olivine without reaction with liquid.

Figures 2A to C show that in the system MgO-FeO-Fe₂O₃-SiO₂ olivine can react with liquid to form pyroxene and spinel when the

oxygen fugacity is buffered. In each of these diagrams is a peritectic point at which olivine dissolves while pyroxene and spinel crystallize during removal of heat. This means that with fractional crystallization on any of these diagrams, a haplobasaltic starting composition that initially precipitates olivine and does not lose it as a precipitating phase along the olivine-pyroxene boundary curve will lose it at the peritectic point by reaction with liquid to form pyroxene and spinel (see also Osborn, 1959, p. 626).

In figures 6A to C this peritectic point on the base of each tetrahedron is the starting point for a univariant line extending into each tetrahedron and ending at invariant points *d*, *d'*, and *d''*, respectively in each diagram. On cooling, liquids along this univariant line in each of the tetrahedra react with olivine to produce protoenstatite and spinel. Thus, when the oxygen fugacity is buffered, haplobasaltic compositions containing CaO also show the reaction relation proposed by Kuno.

Spinel can also participate in the olivine-pyroxene reaction during crystallization at constant total composition. In the system MgO-FeO-Fe₂O₃-SiO₂ (fig. 7), the invariant point *f*, as drawn by Muan and Osborn

TABLE 4
Ultramafic compositions

	1	2	3	4
SiO ₂	43.97	44.6	44.8	46.2
Al ₂ O ₃	2.89	5.5	5.5	
Fe ₂ O ₃	1.04	4.3		
FeO	6.89	7.9		
total Fe as FeO			11.8	13.0
MnO	0.13	0.1	0.1	
MgO	41.11	20.2	20.3	22.4
CaO	2.35	15.8	15.9	18.4
Na ₂ O	0.07	0.5	0.5	
K ₂ O	nil	0.4	0.4	
TiO ₂	0.17	0.7	0.6	
P ₂ O ₅	n.d.			
H ₂ O ⁺	0.35			
H ₂ O ⁻	0.20			
Cr ₂ O ₃	0.50			
NiO	0.21			
CoO	tr.			
CuO	nil			
NaCl	0.09			
Total	99.97	100.0	100.0	100.0

1. Saxonic dunite from St. Paul's Rocks (Tilley, 1947, p. 490).
2. Average composition of ultramafic rocks exposed at Duke Island (Irvine, 1963, p. 45). These values are the average of the two sets of values given by Irvine for the Hall Cove and Judd Harbor outcrop areas, weighted according to the area represented by each set. H₂O not included by Irvine.
3. Same as column 2 with all iron calculated as FeO and the oxide proportions recalculated to 100 percent.
4. Composition of point *m* in figure 6B (71 percent CaMgSi₂O₆, 16 percent Mg₂SiO₄, 13 percent total Fe as FeO).

(1956, fig. 12), is a peritectic point at which olivine dissolves on cooling while pyroxene and spinel crystallize. The univariant line *f-g* extending from this point must therefore also show the same reaction relation at least for some distance into the tetrahedron.

In view of the prevalence in the equilibrium diagrams of the reaction relation of olivine and liquid to form spinel and pyroxene, it is probable that at least some of the mantles of magnetite and hypersthene on olivine phenocrysts in lavas are formed by this reaction.

ULTRAMAFIC ROCKS

Compositions of two types of ultramafic rocks are given in table 4. The analysis in column 1 is representative of the compositions of peridotite nodules in basalts and of peridotites in the central portions of many mountain chains. Column 2 is Irvine's estimated average composition of the exposed rocks of the Duke Island ultramafic complex in Alaska. This complex is similar in overall composition to several other ultramafic bodies in Alaska and British Columbia (Taylor and Noble, 1960; Findlay, ms). As shown in the table, the average exposed rock at Duke Island is richer in CaO and total iron oxide but poorer in MgO than the saxonitic dunite. These differences between the two compositions are reflected in the mineralogy. Ultramafic bodies similar in composition to the Duke Island complex contain the primary minerals olivine, diopside, magnetite, and hornblende, with minor hercynite and anorthite. Rocks similar to the saxonitic dunite characteristically contain the primary minerals olivine, enstatite, diopside, and chrome spinel (Ross, Foster, and Myers, 1954).

Estimated Liquidus and Solidus Temperatures of Peridotites

It may be of interest to comment on the probable liquidus and solidus temperatures of peridotites similar in composition to the saxonitic dunite, particularly in view of recent evidence that some of these peridotites are intruded at high temperatures (MacKenzie, 1960; Smith and MacGregor, 1960; Green, 1964; Challis, 1965). From data on the system forsterite-fayalite, Bowen and Schairer (1936, p. 393) estimated that the liquidus temperature of pure olivine containing 10 to 15 weight percent fayalite is about 1850°C. From their diagrams, the solidus temperature of such an olivine is approximately 1750°C. The purpose here is to indicate the effect of the additional components CaO and Fe₂O₃ on these values.

In the system CaO-MgO-FeO-Fe₂O₃-SiO₂ the assemblage olivine, protoenstatite, diopside, and spinel is a close approximation to the natural assemblage olivine, enstatite, diopside, and chrome spinel. The proportions 65 percent olivine, 25 percent protoenstatite, 8 percent diopside, and 2 percent spinel will be taken as representative of many peridotites, and each of the three silicate phases will be assumed to contain roughly 15 weight percent fayalite, ferrosilite, and hedenbergite, respectively. To a close approximation, this would place the total com-

position in figure 6C, but the total composition does not lie in a region of the diagram where experimental data are available. However, an approximate liquidus temperature obtained by interpolation between the diagrams of Muan and Osborn (1956), Bowen (1914), and this study is about 1700°C. From the known temperature of point x'' in figure 6C and from known solidus temperatures on the base and left side of this tetrahedron, it is estimated that the solidus temperature is in the vicinity of 1250°C. This temperature is the estimated temperature of the liquidus invariant point d'' , and the composition of the first liquid formed on melting would be at d'' . Regardless of the proportions of phases present, the solidus temperature will not change as long as the compositions of the phases remain constant. These considerations suggest that at low pressures, a temperature of approximately 1250°C would be necessary for the existence of peridotite in a partly liquid state. It must be remembered, however, that this conclusion neglects the effect of pressure and the presence of small amounts of other components, particularly Al_2O_3 .

Ultramafic Bodies in Southeastern Alaska and British Columbia

It is possible to discuss in somewhat greater detail ultramafic rocks of the type found in the Duke Island complex, for most of these rocks have compositions that can be closely approximated by mixtures on the join forsterite-diopside-iron oxide. Those who have investigated these bodies in the field are agreed that they formed by crystallization from melts of ultramafic composition. Irvine (1963) suggested that the various ultramafic rocks in the Duke Island complex were produced, except for some of the hornblende pyroxenite forming the marginal zone of the complex, by fractional crystallization of a single ultramafic magma-type. Ruckmick and Noble (1959) proposed that for each major rock type in the Union Bay complex there was a separate magma of like composition. Taylor and Noble (1960) developed this latter theory further and applied it to all of the chemically similar ultramafic bodies in southeastern Alaska. They suggested that fractional melting at depth produced successively more mafic magmas corresponding in composition to hornblende pyroxenite, olivine pyroxenite, peridotite, and dunite. According to this theory, each successive magma was intruded into the center of the previous intrusion to produce a zonal arrangement of rock types that become more mafic toward the center of the complex.

Fractional crystallization.—Point m (fig. 6B) will be taken as a close approximation to the composition of the postulated ultramafic magma from which the ultramafic rocks at Duke Island crystallized. The composition of this point, which lies on the join forsterite-diopside-iron oxide, is shown in column 4 of table 4 and is to be compared with the average ultramafic rock exposed at Duke Island, shown recalculated in column 3. In both cases, the iron is calculated as FeO so as to emphasize the similarity in the total amount of iron present rather than the ratio

of Fe_2O_3 to FeO . The average exposed rock at Duke Island may not be a precise estimate of the original postulated magma. However, this is not of crucial importance in the present context, for the general features of the crystallization path about to be described are not dependent on the exact location of point *m*.

The liquidus temperature of point *m* is about 1450°C , an intrusion temperature more palatable to most geologists than the temperature of 1700°C that was earlier found to be necessary for the existence of an anhydrous peridotite liquid at 1 atm pressure. Since the postulated ultramafic magma at Duke Island would have contained Al_2O_3 , TiO_2 , Na_2O , K_2O , MnO , and H_2O , it is reasonable that it could have been intruded in a completely liquid state at a temperature even lower than 1450°C , possibly 1200 to 1300°C . The intrusion temperature would be further reduced if the ultramafic magma were intruded slightly below its liquidus temperature such that it carried a small amount of olivine crystals suspended in the liquid. It can be deduced from figure 4B that if composition *m* were to consist of about 10 percent olivine crystals and 90 percent liquid, the temperature would be approximately 100°C below the liquidus temperature. Thus, it is reasonable that the postulated ultramafic magma could have been intruded with only a small amount of equilibrium crystals at a temperature as low as 1100 to 1200°C . Such a temperature is compatible with the metamorphic effects believed to have been produced by the ultramafic intrusives in Alaska (Irvine, 1963, p. 43; Taylor and Noble, 1960, p. 180).⁵

The cooling history of composition *m* (fig. 6B) cannot be described in a precise way because of a lack of complete information on the compositions of crystalline phases in equilibrium with all of the liquids. Nevertheless, the data are sufficient for a general discussion of the sequence of events. Upon cooling, olivine rich in magnesium starts to precipitate at the liquidus temperature, about 1450°C . Olivine continues to precipitate as the composition of the liquid travels along the slightly curved path *m-n* through the olivine primary phase volume. At point *n* (about 1330°C) diopside starts to crystallize along with olivine. With continued cooling and continuous removal of the crystalline phases, the composition of the liquid moves on the olivine-diopside boundary surface along the slightly curved path *n-o* toward the univariant line *b'-d'*. At the same time, the compositions of the precipitating olivine and diopside become slightly richer in iron. Just as the liquid reaches point *o* at about 1300°C , the composition of the precipitating olivine is close to point *y'*. The exact composition of the diopside is unknown, but it contains a small amount of iron and must lie near the join $\text{CaMgSi}_2\text{O}_6$ – $\text{CaFeSi}_2\text{O}_6$. In the vicinity of point *x'*, the line *b'-d'* is a reaction line along which olivine dissolves during equilibrium cooling, so with per-

⁵ As emphasized earlier, the data are not sufficient for a discussion of equilibrium processes occurring at high pressures. The intrusion temperature just discussed and the crystallization path to be described below are for low pressures existing in the Earth's crust.

fect fractional crystallization the liquid will not travel along this line but instead will move out along the path $o-p$ in the surface $b'-d'-e'$ as diopside and spinel precipitate together. No significance should be attached to the direction of the line $o-p$. After the liquid leaves point o its exact direction of travel is unknown; it is possible to say only that it moves out onto the divariant surface between diopside and spinel.⁶ On continued cooling, the composition of the liquid moves to parts of the diagram in which no data have been collected.

If the precipitating crystals are assumed to accumulate layer on layer at the bottom of a chamber without retaining any of the liquid phase in the pore spaces, three mineral assemblages would be observed. Going from the bottom to the top of the sequence, these three assemblages and the *approximate* proportions of phases would be: olivine; 10 percent olivine, 90 percent diopside; and 20 percent spinel, 80 percent diopside. If 20 or 30 percent of interprecipitate liquid is trapped and crystallized with the settled minerals, some transitional assemblages would be found. Up to about 20 percent diopside would occur in the olivine layer and small amounts of spinel would occur in the upper part of the olivine plus diopside layer. No olivine would occur in the diopside plus spinel layer. Despite the presence of these transitional assemblages, discontinuities in proportions of phases would remain between the three major assemblages.

The rocks found in the field display several striking similarities to the assemblages discussed above. Most important is the fact that the three most abundant rock-types in several of the intrusive bodies in southeastern Alaska are dunite, olivine pyroxenite, and olivine-free pyroxenite (Irvine, 1963, p. 39). These three rock-types correspond closely to the assemblages discussed above, not only in mineralogy but also in the proportions of minerals. In the Duke Island complex, a large amount of the olivine-free pyroxenite contains 13 to 17 percent (20-24 wt percent) magnetite (Irvine, 1963, p. 39). In the Union Bay complex, a large amount of the pyroxenite also contains a similar, fairly constant percentage of magnetite and is free of olivine except for a few localized areas (Ruckmick and Noble, 1959, p. 992). In the Duke Island complex, olivine pyroxenite typically contains 15 to 30 percent olivine (Irvine, 1963, p. 39), and in the Union Bay complex, the approximate proportions 80 percent diopside, 20 percent olivine prevail throughout the olivine pyroxenite (Ruckmick and Noble, 1959, p. 999). Magnetite occurs only in accessory amounts in the olivine pyroxenite at Duke Island (Irvine, 1965, oral communication) and typically in the amount of 4 to 7 weight percent in the olivine pyroxenite at Union Bay (Ruckmick and Noble, 1959, table 2). As mentioned above, small

⁶ The maximum on the boundary curve between olivine and diopside in the left face suggest that there may be a similar maximum on the univariant line $b'-d'$. If this is the case, some paths of fractional crystallization would move downward and others upward after passing across line $b'-d'$.

amounts of magnetite would be expected in this unit if some inter-precipitate liquid were trapped with the settled minerals.

It is to be noted that the crystallization path deduced above occurs when the oxygen fugacity is buffered. Insufficient data are available for a useful discussion of the crystallization history when the total composition remains constant, but it may be stated in general that the sequence of events would be different. These differences may not be sufficient to rule out crystallization at constant total composition as a possible mode of origin. However, one feature of crystallization behavior in the system $\text{MgO-FeO-Fe}_2\text{O}_3\text{-SiO}_2$ when the total composition remains constant is that the iron contents of olivine and pyroxene increase greatly as cooling proceeds (Muan and Osborn, 1956, p. 136-137). This increase is inhibited when the oxygen fugacity is buffered. It is to be expected that this difference would also occur in the system $\text{CaO-MgO-FeO-Fe}_2\text{O}_3\text{-SiO}_2$. In this connection, it is significant that in the rocks at Duke Island, the Fe/Mg ratio in diopside and olivine increases only slightly in going from dunite to olivine pyroxenite to olivine-free pyroxenite. A slight increase would be expected if the oxygen fugacity of the magma were buffered during crystallization. The abundance of hornblende and mafic pegmatite associated with the ultramafic rocks suggests that the magma contained significant amounts of water, thereby allowing the possibility of buffering of the oxygen fugacity through diffusion of hydrogen.

It is now evident why the $\text{Fe}_2\text{O}_3/\text{FeO}$ ratio was ignored when comparing the composition of point *m* (table 4) with the average ultramafic rock at Duke Island. If crystallization took place under conditions of buffered oxygen fugacity, as argued above, then the final state of oxidation of the magma, as represented by the average composition of the rocks crystallized from it, would be different from the initial oxidation state of the magma.

In using figure 6B for deducing the crystallization path of composition *m*, it was not intended to imply that the oxygen fugacity at which the ultramafic rocks crystallized corresponds to that produced by the equilibrium decomposition of pure CO_2 . It was intended only to illustrate the sequence of events that would occur if the oxygen fugacity were buffered. The approximate oxygen fugacity at which the ultramafic rocks crystallized is suggested by a comparison of the composition of the olivine found in the rocks with olivine compositions determined in this study. In the Union Bay complex, the average composition of the olivine from olivine pyroxenite, expressed in weight percent, is $\text{Fo}_{73}\text{Fa}_{27}$ (Ruckmick and Noble, 1959, fig. 2). This composition is to be compared with an olivine composition of $\text{Fo}_{86}\text{Fa}_{14}$ (neglecting the small amount of calcium) in equilibrium with liquid *x''* in figure 6C. This suggests that the oxygen fugacity at which the olivine pyroxenite crystallized was slightly less than 10^{-6} atm. Unfortunately, the data are not sufficient to determine the complete range of oxygen fugacities over which crystallization paths like *m-n-o-p* in figure 6B would occur, but the available data

give no reason to expect that the ultramafic rocks crystallized at oxygen fugacities outside this range.

The experimental data do not refute the possibility that the ultramafic rocks could be part of a larger differentiated gabbroic intrusion. Addition of *small* amounts of other components to a starting mixture in a simple system can result in the preservation of most of the general features of the *early* stages of fractional crystallization.⁷ That is, the crystallization path of an appropriate basaltic mixture in a nine or ten component system could be very similar, in its early stages, to the crystallization path described above for an ultramafic mixture in the system $\text{CaO-MgO-FeO-Fe}_2\text{O}_3\text{-SiO}_2$. However, there appears to be no reason for believing that the ultramafic rocks formed by precipitation from a gabbroic magma; the field evidence weighs against such an origin (Irvine, 1963, p. 44; Taylor and Noble, 1960, p. 182), and the experimental data provide no reasons for preferring a gabbroic magma.

Fractional melting.—Structural relationships in the Union Bay complex, at least as reported by Ruckmick and Noble (1959, p. 1006-1007), are apparently at variance with a fractional crystallization model (see also Taylor and Noble, 1960, p. 186). With the experimental data presented here, it is not possible to test the alternative hypothesis of fractional melting in the upper mantle presented by Taylor and Noble (1960). Nevertheless, some general considerations on fractional melting are pertinent, and it is believed that these considerations render the fractional melting hypothesis unlikely.

As shown above, the major rock types can be produced by fractional crystallization at low pressures. Thus, in order for fractional melting at high pressures in the upper mantle to be considered a possible mechanism, the compositions of the liquids so produced must essentially duplicate the compositions of settled assemblages produced by fractional crystallization at low pressures. This is considered unlikely for two reasons. First, it is generally true that for any system displaying solid solutions or reaction relationships involving the liquid phase, successive liquids derived by extreme fractional melting cannot duplicate the sequence of crystalline compositions formed by crystal settling during extreme fractional crystallization. Crystallized liquids derived by fractional melting would contain the same crystalline phases precipitated by fractional crystallization, but the assemblages produced and the proportions of phases would be different. Second, even if these differences were small at low pressures, it may be expected that the appearance of new, high-pressure phases in the upper mantle would alter the equilibrium relationships so that a sequence of liquids would be produced whose compositions would be entirely different from settled assemblages produced by fractional crystallization at low pressure.

⁷ See Bowen (1928, p. 299-302) for a discussion on the effect of the addition of 1 percent water to an anhydrous mixture.

In conclusion, the experimental data indicate that fractional crystallization of ultramafic magma under conditions of buffered oxygen fugacity is a chemically suitable mechanism for producing the major rock types observed in the ultramafic bodies in Alaska and British Columbia. Indeed, the degree of correspondence between the rocks expected by fractional crystallization and those found would appear to be more than coincidence. The corroborating field evidence for fractional crystallization at Duke Island (Irvine, 1963) is powerful additional evidence for such a mode of origin, at least for this one ultramafic complex.

APPENDIX A

Experimental Method

Method of thermal study.—The starting materials, "Baker Analyzed" CaCO_3 , MgO , Fe_2O_3 , and silicic acid, were heated as follows: CaCO_3 , 20 hours at 380°C ; MgO , 24 hours at 1350°C ; Fe_2O_3 , 18 hours at 900°C ; and silicic acid, 6 hours at 1350°C . Each composition was made by weighing into an agate mortar the amounts of these compounds necessary to make 10 grams of starting material. This mixture was then ground under acetone for 30 minutes, placed in a platinum crucible, fired in a gas furnace (Denver Fireclay Co., model no. 393) at 1600 to 1650°C for one hour, quenched in water, and ground again in an agate mortar to pass an 80 mesh screen. Mixtures prepared in this way were then used as starting materials for experiments in the quench-furnace. In order to avoid large losses of iron from the mixtures to the platinum crucibles during firing in the gas furnace, crucibles were used that previously had been used repeatedly for melting iron silicate mixtures under these same furnace conditions.

The experiments at high temperatures were carried out in a vertical quench-furnace wound with Pt-20 percent Rh wire, insulated with MgO , and fitted with a three-quarter inch diameter, gas-tight, mullite tube that extended 6 inches below the bottom of the insulating cylinder. For experiments using pure CO_2 and for experiments at 10^{-6} atm oxygen fugacity, the furnace was controlled by a Tagliaubue Celestray controller, whereas for experiments at $10^{-6.68}$ and 10^{-8} atm oxygen fugacity, the furnace was regulated by a Brown Pyr-O-Vane controller. The former controller held the temperature to $\pm 2^\circ\text{C}$ whereas the latter maintained a control of approximately $\pm 5^\circ\text{C}$. The temperature was measured before and after each experiment with a Pt-10 percent Rh thermocouple. This thermocouple was frequently calibrated by placing it at the hot zone of the furnace simultaneously with a second Pt-10 percent Rh thermocouple which was in turn calibrated periodically to $\pm 1^\circ\text{C}$ at the melting points of gold (1062.6°C), diopside (1391.5°C), and pseudowollastonite (1544°C). These calibration points are on the temperature scale of the Geophysical Laboratory (Sosman, 1952, p. 522); the melting point of pseudowollastonite is from Osborn and Schairer (1941, p. 719).

For experiments at $10^{-6.68}$ atm oxygen fugacity, the furnace tube was partly open at the bottom to allow circulation of air over the sample. During experiments at other oxygen fugacities, the gas, either "bone dry" CO_2 or a mixture of "bone dry" CO_2 and electrolytic grade H_2 (supplied by the Matheson Co.), entered the bottom of the furnace tube through the side-arm of a glass quench-cup, which was attached to the mullite tube with a tight-fitting rubber sleeve. A gas mixer identical in principle to that described by Darken and Gurry (1945, p. 1399) was used to supply mixtures of CO_2 and H_2 to the furnace. Dibutyl phthalate was used in the manometers of the gas mixer. The gas flow meters were glass capillary tubes calibrated individually with a wet test meter made by the Precision Scientific Company. The linear flow rate of gas through the furnace was kept near 0.9 centimeters per second in accordance with the recommendations of Darken and Gurry (1945, p. 1400).

When determining the liquidus surfaces at 10^{-6} and 10^{-8} atm oxygen fugacity, it was necessary to adjust the mixing ratio CO_2/H_2 each time an experiment was made

at a different temperature. The proper ratio was determined from a graph of mixing ratio versus temperature at constant oxygen fugacity. This graph was drawn from the equation,

$$r = \frac{K_1 K_2 |\sqrt{p}| + K_1 p}{K_1 K_2 |\sqrt{p}| + (K_2)^2}$$

where r = mixing ratio CO_2/H_2 of the gas started into the furnace, p = desired equilibrium oxygen fugacity at the hot zone of the furnace,

$$K_1 = \frac{(p_{\text{H}_2\text{O}})(p_{\text{CO}})}{(p_{\text{CO}_2})(p_{\text{H}_2})}, \text{ and } K_2 = \frac{(p_{\text{CO}})|\sqrt{p_{\text{O}_2}}|}{(p_{\text{CO}_2})^2}.$$

The equilibrium constants K_1 and K_2 were calculated from the data of Coughlin (1954, tables 27, 28, and 56).

As an indirect check on the entire controlled-atmosphere apparatus, the mixing ratio CO_2/H_2 at which metallic iron and wüstite are in equilibrium at 1303°C was determined and compared with the value obtained by Darken and Gurry (1945, table II). The determination was carried out by suspending a pressed pellet of electrolytic iron from a platinum wire at the hot zone of the furnace at successively higher mixing ratios until wüstite coated the surface of the pellet. The mixing ratio so determined was 0.604 ± 0.007 which corresponds to an oxygen fugacity of $10^{-10.72}$ atm. Darken and Gurry (1945, table II) determined the ratio CO_2/CO in equilibrium with iron and wüstite at this temperature to be 0.297 which, when converted to the mixing ratio CO_2/H_2 using the data of Coughlin (1954, tables 27, 28, and 56), is 0.610. This corresponds to an oxygen fugacity of $10^{-10.71}$ atm.

Since the gas mixture entering the side-arm of the quench-cup came in contact with the quenching liquid before passing through the furnace tube, there was the possibility that vaporization from the quenching liquid might alter the oxygen fugacity of the gas mixture. For this reason dibutyl phthalate, which has a low vapor pressure, was used as the quenching liquid. In order to insure that the dibutyl phthalate did not affect the oxygen fugacity in the furnace, the oxygen fugacity at which iron and wüstite are in equilibrium at 1303°C was determined first with a dry quench-cup and then with dibutyl phthalate in the quench-cup. The results were identical within experimental error at $10^{-10.72}$ atm oxygen fugacity. The method used was the same as that described in the preceding paragraph.

Equilibrium among the crystalline and liquid phases was accomplished very rapidly. For the composition of pure diopside, both glassy and crystalline starting materials yielded the same melting temperature when held at temperature for only 10 minutes. The tendency to form quench crystals increases with iron content, so, other factors being equal, equilibrium between crystals and liquid should occur in less than 10 minutes for all of the compositions studied. Chemical analyses on samples held at temperature for varying lengths of time established that about 3 hours were necessary for a close approach to equilibrium of the ratio $\text{Fe}_2\text{O}_3/(\text{FeO} + \text{Fe}_2\text{O}_3)$. Thus, the reaction between the sample and the gas in the furnace controlled the rate of approach to equilibrium. As an added precaution, both glassy and crystalline starting materials were used for certain of the compositions with liquidus temperatures lower than the melting point of pure diopside. Experiments lasting 3 hours or more always yielded the same phase assemblages with both starting materials. Most of the samples were held at temperature for more than 3 hours as indicated in appendices B, C, D, and E.

In the initial stages of the work, phase identification was performed microscopically in both transmitted and reflected light, with occasional verification by powder X-ray diffraction. Later, almost all phase identification was carried out microscopically with reflected light. This was necessary for distinguishing spinel from magnesiowüstite, but it was found also to be the best technique for distinguishing olivine from diopside when one or both were present in trace amounts. When the surface to be observed was polished on a soft wheel, olivine displayed more relief than diopside. Also, equilibrium crystals of diopside were usually encased in a thin rim of quench crystals whereas equilibrium crystals of olivine were not. These rims displayed a reflectivity different from the surrounding glass or the equilibrium diopside crystals which they encased.

Chemical analyses.—During the firing of the starting mixtures and during the experiments in the quench-furnace there was the possibility of losing iron from the

mixtures to the platinum containers. It was therefore necessary to analyze for FeO and total iron after the experiments in the quench-furnace. Ferrous iron was determined with potassium permanganate and total iron with stannous chloride and potassium dichromate, but the standard procedures were slightly modified due to an inability to separate completely the platinum envelope from the sample prior to analysis.

The exact procedure was as follows: The entire sample including the platinum envelope was crushed in an agate mortar to pass a 100 mesh screen. This removed most of the fragments of the platinum envelope. The resulting sample, weighing 0.1 to 0.2 grams, was weighed into a 50 cubic centimeter platinum crucible. A few drops of freshly boiled, distilled water were then added to disperse the sample. In an auxiliary platinum crucible, 5 milliliters freshly boiled, distilled water, 5 milliliters concentrated H_2SO_4 , and 5 milliliters 48 percent HF were mixed together and brought to boiling temperature. This hot acid mixture was then poured into the crucible containing the sample, covered with a carefully flattened lid, and immediately (about 15 seconds) brought to a full boil as evidenced by the continuous evolution of steam. The sample was boiled in this way for 10 to 12 minutes and then plunged, while still boiling, into a solution containing 5 milliliters concentrated H_2SO_4 and 200 milliliters of 5 percent boric acid freshly made with boiled distilled water. This solution was then immediately titrated with approximately 0.03 N KMnO_4 . Platinum fragments that passed through the 100 mesh screen were removed by filtering; the filter paper was then washed with 1:10 H_2SO_4 and ignited in a platinum crucible. A few drops of HF were added to dissolve any remaining silica gel, and the weight of the remaining platinum fragments was subtracted from the weight of the sample. After evaporating the filtered solution to about 200 milliliters and adding about 100 milliliters concentrated HCl, the solution was heated to just below boiling temperature, reduced with excess stannous chloride solution, oxidized by adding a few grains of solid $\text{K}_2\text{Cr}_2\text{O}_7$, reduced again with excess stannous chloride solution, and finally titrated potentiometrically with approximately 0.05 N $\text{K}_2\text{Cr}_2\text{O}_7$. As soon as the excess stannous chloride is titrated there is the possibility of oxidizing the ferrous iron if the solution is allowed to stand. In order to avoid low total iron results due to this effect, the ferrous iron was titrated as rapidly as possible by turning the stopcock wide open immediately after reaching the stannous chloride end point. Only the last milliliter of $\text{K}_2\text{Cr}_2\text{O}_7$ was added slowly so as to obtain a sharp end point.

Table 5 presents a comparison of the iron determinations in this work with those by other analysts and methods. Mixture 28 is one of the starting compositions prepared for this study as described previously. The 13 FeO determinations on this mixture were performed periodically throughout this work as a continuous check on the activity of the KMnO_4 . The method used for mixture 28 and for W-1 basalt was identical to that described above except that it was not necessary to filter off any platinum fragments. Ingamells also used essentially the same method on mixture 28 except that he took precautions to remove any platinum that might be in the sample by precipitation with H_2S prior to the determination of total iron. The pyrophosphate method he used on mixture 28 is described by Ingamells (1960).

There were several sources of uncertainty in the analyses of the products of equilibrium experiments that did not occur in the determinations shown in table 5. One of these was the transfer of iron from the charges to the envelopes during experiments in the quench-furnace. This would have presented no problem if every sample were analyzed, but it was impossible simultaneously to retain all of each sample for analysis and also make a polished section for determination of the phases. This difficulty was minimized by making the samples for analysis approximately the same weight relative to their platinum envelopes as the samples for phase identification (0.1-0.2 grams of sample in a platinum envelope weighing about 0.03 grams).

Another possible source of error was the change in oxidation state of part of the iron during quenching. It was not possible to be certain that the oxidation state did not change during quenching. Nevertheless, an indication of the errors to be expected was obtained by quenching identical samples in media with different oxygen fugacities. The results are shown in table 6. Samples held at 10^{-6} and 10^{-8} atm oxygen fugacity and quenched in water were not exposed to air but were dropped through the gas supplied to the furnace. For comparison, duplicate samples were quenched only in the gas supplied to the furnace by dropping the sample into a dry copper saucer.

TABLE 5
Iron determinations by different analysts and methods

Sample	FeO (wt percent)	Total Fe as Fe ₂ O ₃ (wt percent)*	Method	Analyst
Mixture 28**	26.03±0.11†	62.24±0.05‡	KMnO ₄ + K ₂ Cr ₂ O ₇	D. C. Presnall
"	25.84	62.59	"	C. O. Ingamells
"	26.10	—	Pyrophosphate	C. O. Ingamells
W-1 basalt	8.71	11.03	KMnO ₄ + K ₂ Cr ₂ O ₇	D. C. Presnall
"	8.71	11.06	"	Ingamells and Suhr (1963, table 3)
"	8.71	11.09	"	Goldich and Oslund (1956, table 2)
"	8.75	—	Pyrophosphate	Ingamells (1960, table I)

* Total Fe as Fe₂O₃ = (wt percent FeO)(1.1114) + wt percent Fe₂O₃.

** Exclusive of iron oxides, this mixture consists of CaMgSi₂O₆ and Mg₂SiO₄ in the ratio by weight of 37:3.

† Mean deviation based on 13 determinations (sample size approximately 0.13 g).

‡ Mean deviation based on 5 determinations (sample size approximately 0.13 g).

Column 3 of table 6 shows that for experiments at 10⁻⁶ and 10⁻⁸ atm oxygen fugacity, the oxidation state of the sample was not measurably affected by the different quenching methods. For experiments at 10^{-0.08} atm oxygen fugacity, the two quenching techniques gave reproducible but different results. It was impossible to tell which, if either, of the quenching techniques yielded the correct analysis. However, as shown in table 6, the difference in the quantity (Fe₂O₃)(100)/(FeO + Fe₂O₃) is only about 2 percent. For the analyses reported in appendices B, C, D, and E, the samples were quenched dry in the gas supplied to the furnace.

For samples containing less than about 15 percent total iron oxide, the quantity (Fe₂O₃)(100)/(FeO + Fe₂O₃) was more uncertain due to a small KMnO₄ titer for FeO. For experiments at 10^{-0.08} atm oxygen fugacity an additional difficulty was found in determining FeO in samples low in total iron oxide. For these samples, the scatter on duplicate experiments exceeded that to be expected from a small titer, and no trustworthy values could be obtained. No explanation for this abnormal scatter was discovered. However, total iron determinations on these samples were reproducible and are therefore reported. Since the total iron percentages are small they would be in error by only a slight amount due to an erroneous FeO determination.

It was thought that small fragments of the platinum envelope left in the sample after screening might introduce an error due to acid attack on the iron alloyed with the platinum. To check this, a starting mixture of high iron oxide content was held at 10⁻⁸ atm oxygen fugacity so as to produce an envelope heavily alloyed with iron. This sample was crushed and dissolved in the normal way except it was not screened to remove platinum fragments. After the sample was dissolved, the platinum fragments were filtered off, examined under a binocular microscope to be sure they were free of attached iron oxide, and added to a weighed sample of mixture 28. This sample was then dissolved and analyzed for FeO in the normal way. The result, 26.13 percent FeO, is identical within experimental error to the other analyses of mixture 28 (see table 5). Therefore, no measurable amount of iron was dissolved from the added fragments of platinum-iron alloy. The platinum fragments were subsequently analyzed by E. W. White on an electron probe and found to contain 22 ± 2 percent iron by weight. Further, he found that the iron concentration was uniform throughout the thickness of the foil. If the iron had been partially leached out by the acids, its concentration would be expected to decrease near the surface.

Method of determination of olivine compositions.—Compositions of olivines were determined by measuring their β indices of refraction and d_{100} values. A Zeiss Abbé

TABLE 6
Dependence of oxidation state of iron on method of quenching

Mixture number	Oxygen fugacity (atm)	Quenching medium	Composition of sample in wt percent after quenching, iron oxides by analysis			Temp (°C)	Time (hrs)	Mixing ratio, CO ₂ /H ₂
			$\left(\frac{\text{Fe}_2\text{O}_3}{\text{FeO} + \text{Fe}_2\text{O}_3} \right) (100)$	total Fe as FeO*	CaMgSi ₂ O ₆			
1	10 ^{-0.08}	air	82.2	38.2	61.8	1452	9	—
1	10 ^{-0.08}	water	80.5	38.0	62.0	1451	11	—
2	10 ⁻⁶	CO ₂ /H ₂ = 19.10	34.7	57.1	42.9	1403	10	19.10
2	10 ⁻⁶	water	34.0	57.3	42.7	1401	9	19.10
3	10 ⁻⁸	CO ₂ /H ₂ = 4.06	21.7	55.8	44.2	1354	11	4.06
3	10 ⁻⁸	water	21.9	55.5	44.5	1352	13	4.06

$$* \text{ Total Fe as FeO} = \left(\frac{\text{g FeO} + (\text{g Fe}_2\text{O}_3)(0.8998)}{\text{g FeO} + (\text{g Fe}_2\text{O}_3)(0.8998) + \text{g CaMgSi}_2\text{O}_6} \right) (100).$$

refractometer thermostated with water kept within a temperature variation of $\pm 0.3^\circ\text{C}$ was used to calibrate the indices of refraction of the immersion liquids to five significant figures. These liquids were then used to determine the β index of refraction of each olivine to four significant figures. In each case, the temperature of the oil on the microscope stage was measured, and an appropriate correction applied to the index of refraction determined with the refractometer. As an indirect check on the procedure, the β index of refraction of synthetically made forsterite was found by this method to be 1.651. Bowen and Schairer (1935, table V) obtained the value 1.6507, also on synthetic material. The forsterite was made by firing the required amounts of "Baker Analyzed" MgO and dehydrated silicic acid together at 1400°C for two weeks with several intermediate grindings. This procedure yielded a product that contained a trace of enstatite as determined by powder X-ray diffraction and a trace of at least two other phases besides forsterite as determined microscopically. However, since the phase diagram for MgO-SiO_2 (Bowen and Andersen, 1914) shows no solid solution in forsterite, the β index of refraction should be correct even though reaction was not complete.

The d_{130} values of the olivines were measured with $\text{CuK}\alpha$ radiation using the (111) peak of silicon as an internal standard. The unit cell dimension of silicon was taken at 5.43062 \AA (Parrish, 1953). Each recorded d_{130} is the average of two forward and two reverse tracings made at $1/4^\circ$ per minute on a Norelco X-ray diffractometer. This procedure was indirectly checked by determining in the same way the d_{130} of the synthetic forsterite described in the previous paragraph. The result, 2.766, is in agreement with the value 2.7661 obtained by Yoder and Sahama (1957, p. 486) on synthetic material.

APPENDIX B

Experiments at $10^{-6.68}$ atm oxygen fugacity

Composition of mixture (wt percent, iron oxides by analysis)				Temp ($^\circ\text{C}$)	Time (hrs)	Phases present‡
Mg_2SiO_4	$\text{CaMgSi}_2\text{O}_6$	Total Fe as FeO^*	$\frac{(\text{Fe}_2\text{O}_3)(100)}{\text{FeO} + \text{Fe}_2\text{O}_3}$ at liquidus temp**			
0	90.7	9.3	¶	1354	9	†
				1361	10	l
				1352	3	diop + l
				1300	10	diop + l
				1292	23	diop + sp + l
0	81.2	18.8	87.4	1311	34	
				1314	10	l
				1306	24	diop + l
				1292	23	diop + sp + l
0	71.6	28.4	85.2	1382	27	
				1376	6	l
				1368	8	sp + l
				1300	10	sp + l
				1293	21	diop + sp + l
0	61.8	38.2	82.2	1452	9	
				1456	3	l
				1446	3	sp + l
				1289	6	sp + l
				1282	24	diop + sp + l
0	51.8	48.2	79.9	1490	7	
				1494	3	l
				1482	3	sp + l
				1271	47	sp + l
				1263	60	diop + sp + l
				1254	64	diop + sp +
						hem + l

Composition of mixture (wt percent, iron oxides by analysis)						
Mg ₂ SiO ₄	CaMgSi ₂ O ₆	Total Fe as FeO*	(Fe ₂ O ₃) (100) FeO + Fe ₂ O ₃	Temp (°C)	Time (hrs)	Phases present‡
			at liquidus temp**			
0	41.7	58.3	78.7	1523	10	
				1527	3	l
				1519	3	sp + l
				1278	21	sp + l
				1266	3	sp + hem + l
0	31.7	68.3	77.8	1545	6	
				1545	3	l
				1535	3	sp + l
0	21.3	78.7	76.8	1552	11	
				1560	3	l
				1547	3	sp + l
				1333	3	sp + l
				1320	5	sp + hem + l
0	10.0	90.0	75.9	1566	8	
				1579	3	l
				1566	9	sp + l
				1350	23	sp + hem + l
				1266	3	sp + hem + l
0	5.8	94.2	74.9	1575	4	
				1586	3	l
				1572	3	sp + l
4.0	88.1	7.9	¶	1354	24	
				1362	24	l
				1347	23	diop + l
4.0	83.6	12.4	¶	1341	12	
				1346	3	l
				1335	3	ol + l
20.5	66.4	13.1	¶	1494	13	
				1499	3	l
				1486	3	ol + l
10.3	77.1	12.6	¶	1406	11	
				1411	3	l
				1399	3	ol + l
5.0	80.8	14.2	¶	1348	21	
				1351	3	l
				1346	3	ol + l
2.0	77.1	20.9	87.0	1319	19	
				1327	3	l
				1316	3	ol + l
0.5	78.1	21.4	87.2	1319	10	
				1320	4	l
				1315	4	sp + l
10.3	67.0	22.7	84.7	1404	11	
				1411	3	l
				1399	3	ol + l
17.4	55.4	27.2	84.3	1446	7	
				1457	10	l
				1445	7	ol + l

Composition of mixture (wt percent, iron oxides by analysis)						
Mg ₂ SiO ₄	CaMgSi ₂ O ₆	Total Fe as FeO*	$\frac{(\text{Fe}_2\text{O}_3)(100)}{\text{FeO} + \text{Fe}_2\text{O}_3}$	Temp (°C)	Time (hrs)	Phases present†
			at liquidus temp**			
14.4	56.7	28.9	84.7	1442	9	
				1449	4	l
				1442	4	sp + l
30.1	38.1	31.8	82.0	1534	12	
				1542	3	l
				1528	3	ol + l
				1518	3	ol + sp + l
9.2	57.4	33.4	83.3	1450	11	
				1455	10	l
				1442	8	sp + l
15.4	46.4	38.2	81.9	1505	9	
				1512	3	l
				1495	3	sp + l
10.7	32.2	57.1	79.2	1538	8	
				1544	5	l
				1531	3	sp + l

$$* \text{ Total Fe as FeO} = \left(\frac{\text{g FeO} + (\text{g Fe}_2\text{O}_3)(0.8998)}{\text{g FeO} + (\text{g Fe}_2\text{O}_3)(0.8998) + \text{wt of all other oxides}} \right) (100).$$

Samples for analysis of FeO and total iron were made at the estimated liquidus temperature for each composition as determined by the phases found in previous un-analyzed samples. Since the platinum envelope removes different amounts of iron from the charge at different temperatures, the value for total Fe as FeO is precisely correct only at the temperature of the sample analyzed. Mean deviation of replicate determinations is 0.1 wt percent based on 10 different samples analyzed two to six times.

** This quantity is strongly dependent on temperature and is correct for a given mixture only at the temperature of the analyzed sample.

† All samples for analysis were entirely consumed, and it was not possible to determine the phases present.

‡ diop = diopside, sp = spinel, mw = magnesiowüstite, hem = hematite, ol = olivine, l = liquid.

¶ No value reported due to poor reproducibility. See appendix A.

APPENDIX C§

Experiments using pure CO₂

Composition of mixture (wt percent, iron oxides by analysis)						
Mg ₂ SiO ₄	CaMgSi ₂ O ₆	Total Fe as FeO§§	$\frac{(\text{Fe}_2\text{O}_3)(100)}{\text{FeO} + \text{Fe}_2\text{O}_3}$	Temp (°C)	Time (hrs)	Phases present
			at liquidus temp			
0	90.9	9.1	75.3	1352	10	
				1364	10	l
				1350	12	diop + l
0	81.2	18.8	77.5	1311	9	
				1317	12	l
				1302	14	diop + l

Composition of mixture (wt percent,
iron oxides by analysis)

Mg ₂ SiO ₄	CaMgSi ₂ O ₆	Total Fe as FeO§§	$\frac{(\text{Fe}_2\text{O}_3)(100)}{\text{FeO} + \text{Fe}_2\text{O}_3}$		Temp (°C)	Time (hrs)	Phases present
			at liquidus temp				
0	71.8	28.2	71.3	1388	9		
				1402	10	l	
				1379	11	sp + l	
0	61.9	38.1	69.0	1450	12		
				1459	11	l	
				1437	10	sp + l	
0	52.2	47.8	66.6	1491	10		
				1505	8	l	
				1484	11	sp + l	
0	41.8	58.2	64.9	1516	11		
				1532	10	l	
				1505	8	sp + l	
0	21.2	78.8	60.3	1548	10		
				1564	10	l	
				1541	10	sp + l	
0	10.6	89.4	60.0	1566	8		
				1564	10	l	
				1541	10	sp + l	
4.0	88.3	7.7	74.3	1354	13		
				1357	11	l	
				1345	9	diop + l	
4.0	83.7	12.3	76.3	1339	10		
				1350	7	l	
				1341	7	ol + l	
				1328	12	ol + diop + l	
10.3	77.2	12.5	72.3	1410	12		
				1422	8	l	
				1398	8	ol + l	
20.5	66.7	12.8	66.1	1493	9		
				1502	10	l	
				1484	8	ol + l	
2.0	77.1	20.9	76.5	1319	10		
				1328	12	l	
				1312	13	ol + l	
				1305	22	ol + l	
				1301	20	ol + diop + sp + l	
				1297	25	diop + sp + l	
14.5	56.8	28.7	69.7	1441	10		
				1449	15	l	
				1430	8	ol + sp + l	
30.2	38.2	31.6	65.6	1549	7		
				1560	9	l	
				1540	13	ol + l	
9.2	57.5	33.3	69.8	1447	12		
				1449	15	l	
				1430	8	sp + l	

Composition of mixture (wt percent,
iron oxides by analysis)

Mg ₂ SiO ₄	CaMgSi ₂ O ₆	Total Fe as FeO§§	$\frac{(\text{Fe}_2\text{O}_3)(100)}{\text{FeO} + \text{Fe}_2\text{O}_3}$		Temp (°C)	Time (hrs)	Phases present
			at liquidus temp				
15.5	46.7	37.8	68.0		1494	12	
					1502	10	1
					1484	8	sp + 1
15.8	24.3	59.9	63.6		1543	9	
					1560	9	1
					1540	13	sp + 1

§ In appendix B, footnotes **, †, ‡, and all but the last sentence of footnote * apply to this appendix also.

§§ Mean deviation of replicate determinations is 0.2 wt percent based on five different samples analyzed twice.

APPENDIX D§

Experiments at 10⁻⁶ atm oxygen fugacity

Composition of mixture (wt percent,
iron oxides by analysis)

Mg ₂ SiO ₄	CaMgSi ₂ O ₆	Total Fe as FeO§§	$\frac{(\text{Fe}_2\text{O}_3)(100)}{\text{FeO} + \text{Fe}_2\text{O}_3}$		Temp (°C)	Time (hrs)	Mixing ratio, CO ₂ /H ₂	Phases present	
			at liquidus temp						
0	92.2	7.8	28.8		1350	18	35.8		
						1358	9	32.5	1
						1346	8	37.2	diop + 1
0	81.7	18.3	42.3§§§		1316	10	55.3		
						1324	10	49.9	1
						1308	11	58.5	diop + 1
0	77.2	22.8	36.0		1315	10	55.3		
						1320	8	51.2	1
						1308	11	58.5	sp + 1
0	72.5	27.5	34.8		1334	10	43.9		
						1339	9	40.7	1
						1324	10	49.9	sp + 1
0	53.2	46.8	33.4		1388	9	22.5		
						1395	7	21.0	1
						1383	12	24.2	sp + 1
0	42.9	57.1	34.7		1403	10	19.1		
						1408	14	17.8	1
						1399	8	20.0	sp + 1
0	32.6	67.4	36.0		1409	10	17.4		
						1416	6	15.9	1
						1399	8	20.0	sp + 1
0	22.0	78.0	36.2		1416	11	16.3		
						1422	13	14.9	1
						1408	14	17.8	sp + 1
0	11.0	89.0	37.5		1425	10	14.7		
						1429	10	13.9	1
						1422	13	14.9	sp + 1

Composition of mixture (wt percent, iron oxides by analysis)				Temp (°C)	Time (hrs)	Mixing ratio, CO ₂ /H ₂	Phases present
Mg ₂ SiO ₄	CaMgSi ₂ O ₆	Total Fe as FeO§§	$\frac{(\text{Fe}_2\text{O}_3)(100)}{\text{FeO} + \text{Fe}_2\text{O}_3}$ at liquidus temp				
4.0	89.2	6.8	24.7	1361	22	30.8	
				1367	8	28.6	l
				1357	9	32.4	diop + l
4.1	84.6	11.3	30.5	1347	9	37.7	
				1354	6	34.0	l
				1336	12	41.8	ol + diop + l
10.4	78.2	11.4	24.3	1419	8	16.1	
				1424	11	14.9	l
				1410	11	17.4	ol + l
20.8	67.6	11.6	17.5	1516	10	5.85	
				1524	5	5.43	l
				1509	5	6.28	ol + l
2.1	79.2	18.7	29.7	1354	11	34.0	
				1354	6	34.0	l
				1336	12	41.8	ol + l
9.4	58.3	32.3	26.7	1433	12	13.6	
				1440	12	12.5	l
				1424	11	14.9	ol + l
16.1	48.1	35.8	25.4	1484	11	7.98	
				1490	10	7.62	l
				1476	11	8.57	ol + l
4.2	47.5	48.3	34.2	1394	10	21.0	
				1401	7	19.1	l
				1393	7	21.4	sp + l
6.4	40.7	52.9	35.5	1396	11	20.5	
				1406	13	20.0	l
				1395	8	22.4	ol + l
				1389	11	24.2	ol + sp + l
3.2	39.8	57.0	34.6	1398	8	20.0	
				1406	13	20.0	l
				1395	8	22.4	sp + l
11.0	32.9	56.1	33.5	1440	8	12.5	
				1446	9	11.7	l
				1434	10	13.3	ol + l
16.2	24.9	58.9	31.9	1483	9	7.98	
				1490	10	7.62	l
				1476	11	8.57	ol + l
				1461	7	10.1	ol + l
				1440	12	12.5	ol + mw + l
5.4	35.6	59.0	35.5	1400	10	19.5	
				1415	7	18.2	l
				1400	11	21.0	mw + l
6.4	32.2	61.4	36.0	1410	7	17.4	
				1425	9	15.9	l
				1409	10	19.1	mw + l

Composition of mixture (wt percent,
iron oxides by analysis)

Mg ₂ SiO ₄	CaMgSi ₂ O ₆	Total Fe as FeO§§	$\frac{(\text{Fe}_2\text{O}_3)(100)}{\text{FeO} + \text{Fe}_2\text{O}_3}$		Temp (°C)	Time (hrs)	Mixing ratio, CO ₂ /H ₂	Phases present
			at liquidus temp					
22.1	16.6	61.3	28.1		1559	7	4.06	
					1567	5	3.80	1
					1548	5	4.42	mw + 1
10.9	27.1	62.0	34.3		1444	11	11.9	
					1456	7	10.5	1
					1443	11	12.2	mw + 1
4.3	23.9	71.8	36.0		1423	8	14.9	
					1434	9	14.9	1
					1422	14	15.2	mw + 1
8.8	18.7	72.4	34.6		1458	9	10.3	
					1459	10	10.1	1
					1443	11	12.2	mw + 1
3.2	10.6	86.3	35.6		1452	10	11.0	
					1459	10	10.1	1
					1446	9	11.7	mw + 1
11.2	0	88.8	29.1		1550	6	4.35	
					1560	5	4.00	1
					1542	8	4.58	mw + 1

§ In appendix B, footnotes **, †, ‡, and all but the last sentence of footnote * apply to this appendix also.

§§ Mean deviation of replicate determinations is 0.2 wt percent based on 14 different samples analyzed from two to three times.

§§§ This value appears too high, and the sample may have been oxidized during quenching or analysis.

APPENDIX E§

Experiments at 10⁻⁸ atm oxygen fugacity

Composition of mixture (wt percent,
iron oxides by analysis)

Mg ₂ SiO ₄	CaMgSi ₂ O ₆	Total Fe as FeO§§	(Fe ₂ O ₃) (100)		Temp (°C)	Time (hrs)	Mixing ratio, CO ₂ /H ₂	Phases present
			FeO + Fe ₂ O ₃	at liquidus temp				
0	94.0	6.0	9.8		1350	10	4.15	
					1357	10	3.85	1
					1345	9	4.35	diop + 1
0	84.3	15.7	13.6		1355	10	3.98	
					1361	9	3.62	1
					1351	9	4.15	ol + 1
0	74.3	25.7	14.2		1368	11	3.44	
					1377	22	3.12	1
					1361	9	3.62	ol + 1
0	64.2	35.8	15.0		1368	10	3.44	
					1376	17	3.11	1
					1362	22	3.62	ol + 1
0	55.9	44.1	17.9		1353	11	3.90	
					1362	22	3.62	1

Composition of mixture (wt percent, iron oxides by analysis)				Temp (°C)	Time (hrs)	Mixing ratio, CO ₂ /H ₂	Phases present
Mg ₂ SiO ₄	CaMgSi ₂ O ₆	Total Fe as FeO§§	$\frac{(\text{Fe}_2\text{O}_3)(100)}{\text{FeO} + \text{Fe}_2\text{O}_3}$ at liquidus temp				
0	44.2	55.8	21.7	1354	11	4.07	
				1357	10	3.85	1
				1345	9	4.39	mw + 1
0	33.4	66.6	20.5	1391	10	2.76	
				1400	10	2.51	1
				1387	9	2.81	mw + 1
0	22.6	77.4	19.7	1401	11	2.51	
				1416	10	2.12	1
				1400	10	2.51	mw + 1
0	11.3	88.7	21.1	1403	9	2.44	
				1404	10	2.37	1
4.0	90.0	6.0	14.4	1362	9	3.66	
				1367	11	3.44	1
				1358	9	3.82	diop + ol + 1
4.1	85.6	10.3	12.7	1371	8	3.30	
				1377	22	3.12	1
				1366	9	3.44	ol + 1
10.7	80.2	9.1	9.8	1437	14	1.80	
				1446	10	1.68	1
				1431	9	1.88	ol + 1
21.7	70.5	7.8	9.5	1522	9	0.984	
				1526	10	0.927	1
				1513	10	1.02	ol + 1
4.4	77.3	18.3	11.8	1402	10	2.39	
				1412	10	2.22	1
				1399	10	2.55	ol + 1
10.4	64.5	25.1	10.7	1464	11	1.44	
				1472	12	1.36	1
				1461	10	1.51	ol + 1
17.7	53.3	29.0	10.2	1507	11	1.08	
				1514	10	1.02	1
				1497	11	1.14	ol + 1
11.9	35.8	52.3	15.4	1453	10	1.59	
				1461	10	1.51	1
				1446	10	1.68	ol + 1
18.9	28.9	52.2	14.6	1505	9	1.08	
				1514	10	1.02	1
				1497	11	1.14	ol + mw + 1
10.1	21.5	68.4	16.3	1497	13	1.16	
				1501	12	1.09	1
				1489	10	1.23	mw + 1
13.0	0	87.0	15.3	1518	10	0.984	
				1526	10	0.927	1
				1513	10	1.02	mw + 1

§ In appendix B, footnotes **, †, ‡, and all but the last sentence of footnote * apply to this appendix also.

§§ Mean deviation of replicate determinations is 0.6 wt percent based on 10 different samples analyzed from two to five times.

REFERENCES

- Anderson, C. A., 1933, Volcanic history of Glass Mountain, northern California: *Am. Jour. Sci.*, 5th ser., v. 26, p. 485-506.
- 1941, Volcanoes of the Medicine Lake Highland, California: *Calif. Univ. Dept. Geol. Sci. Bull.*, v. 25, p. 347-422.
- Aoki, Ken-ichiro, 1959, Petrology of alkali rocks of the Iki Islands and Higashimatsuura district, Japan: *Tohoku Univ. Sci. Rept.*, ser. 3, v. 6, p. 261-310.
- Asayama, Tetsuji, 1953, On the radioactivity of rocks in Japan and vicinity; I. Radium content of volcanic rocks: *Kyoto Tech. Univ. Fac. Indus. Arts Mem., Sci. and Technology*, v. 2-B, p. 53-69.
- Bowen, N. L., 1914, The ternary system: diopside-forsterite-silica: *Am. Jour. Sci.*, 4th ser., v. 38, p. 207-264.
- 1915, The crystallization of haplobasaltic, haplodioritic, and related magmas: *Am. Jour. Sci.*, 4th ser., v. 40, p. 161-185.
- 1928, The evolution of the igneous rocks: Princeton, New Jersey, Princeton Univ. Press, 334 p.
- 1941, Certain singular points on crystallization curves of solid solutions: [U.S.] *Natl. Acad. Sci. Proc.*, v. 26, no. 6, p. 301-309.
- 1954, Experiment as an aid to the understanding of the natural world: *Acad. Nat. Sci. Philadelphia Proc.*, v. 106, p. 1-12.
- Bowen, N. L., and Andersen, Olaf, 1914, The binary system MgO-SiO_2 : *Am. Jour. Sci.*, 4th ser., v. 37, p. 487-500.
- Bowen, N. L., and Schairer, J. F., 1935, The system, MgO-FeO-SiO_2 : *Am. Jour. Sci.*, 5th ser., v. 29, p. 151-217.
- 1936, The problem of the intrusion of dunite in the light of the olivine diagram: *Internat. Geol. Cong.*, 16th, Washington 1933, Rept., v. 1, p. 391-396.
- Bowen, N. L., Schairer, J. F., and Posnjak, Eugen, 1933a, The system, $\text{Ca}_2\text{SiO}_4\text{-Fe}_2\text{SiO}_4$: *Am. Jour. Sci.*, 5th ser., v. 25 p. 273-297.
- 1933b, The system, CaO-FeO-SiO_2 : *Am. Jour. Sci.*, 5th ser., v. 26, p. 193-284.
- Buddington, A. F., and Lindsley, D. H., 1964, Iron-titanium oxide minerals and synthetic equivalents: *Jour. Petrology*, v. 5, p. 310-357.
- Carmichael, I. S. E., 1964, The petrology of Thingmuli, a Tertiary volcano in eastern Iceland: *Jour. Petrology*, v. 5, p. 435-460.
- Challis, G. A., 1965, High-temperature contact metamorphism at the Red Hills ultramafic intrusion-Wairau Valley-New Zealand: *Jour. Petrology*, v. 6, p. 395-419.
- Chayes, Felix, 1964, A petrographic distinction between Cenozoic volcanics in and around the open oceans: *Jour. Geophys. Research*, v. 69, p. 1573-1588.
- Chinner, G. A., 1960, Pelitic gneisses with varying ferrous/ferric ratios from Glen Clova, Angus, Scotland: *Jour. Petrology*, v. 1, p. 178-217.
- Coughlin, J. P., 1954, Contributions to the data on theoretical metallurgy. XII. Heats and free energies of formation of inorganic oxides: *U.S. Bur. Mines Bull.* 542, 80 p.
- Darken, L. S., and Gurry, R. W., 1945, The system iron-oxygen. I. The wüstite field and related equilibria: *Am. Chem. Soc. Jour.*, v. 67, p. 1398-1412.
- 1946, The system iron-oxygen. II. Equilibrium and thermodynamics of liquid oxide and other phases: *Am. Chem. Soc. Jour.*, v. 68, p. 798-816.
- Engel, A. E. J., and Engel, C. G., 1964, Igneous rocks of the East Pacific Rise: *Science*, v. 146, p. 477-485.
- Engel, A. E. J., Engel, C. G., and Havens, R. G., 1965, Chemical characteristics of oceanic basalts and the upper mantle: *Geol. Soc. America Bull.*, v. 76, p. 719-734.
- Eugster, H. P., 1957, Heterogeneous reactions involving oxidation and reduction at high pressures and temperatures: *Jour. Chem. Physics*, v. 26, p. 1760-1761.
- 1959, Reduction and oxidation in metamorphism, in Abelson, P. H., ed., *Researches in geochemistry*: New York, John Wiley and Sons, p. 397-426.
- Fenner, C. N., 1929, The crystallization of basalts: *Am. Jour. Sci.*, 5th ser., v. 18, p. 225-253.
- Ferguson, J. B., and Merwin, H. E., 1919, The ternary system CaO-MgO-SiO_2 : *Am. Jour. Sci.*, 4th ser., v. 48, p. 81-123.
- Findlay, D. C., ms, 1963, Petrology of the Tulameen ultramafic complex, Yale district, British Columbia: Ph.D. thesis, Queen's University, 407 p.
- Fudali, R. F., 1965, Oxygen fugacities of basaltic and andesitic magmas: *Geochim. et Cosmochim. Acta*, v. 29, p. 1063-1075.

- Goldich, S. S., and Oslund, E. H., 1956, Composition of Westerly granite G-1 and Centerville diabase W-1: *Geol. Soc. America Bull.*, v. 67, p. 811-815.
- Green, D. H., 1964, The petrogenesis of the high-temperature peridotite intrusion in the Lizard area, Cornwall: *Jour. Petrology*, v. 5, p. 134-188.
- Hirokawa, Osamu, and Suyama, T., 1955, Chemical changes of the volcanic rocks due to decompositions (in Japanese): *Japan Geol. Survey Bull.*, v. 6, no. 7, p. 445-450.
- Ingamells, C. O., 1960, A new method for "ferrous iron" and "excess oxygen" in rocks, minerals, and oxides: *Talanta*, v. 4, p. 268-273.
- Ingamells, C. O., and Suhr, N. H., 1963, Chemical and spectrochemical analysis of standard silicate samples: *Geochim. et Cosmochim. Acta*, v. 27, p. 897-910.
- Irvine, T. N., 1963, Origin of the ultramafic complex at Duke Island, southeastern Alaska: *Mineralog. Soc. America Spec. Paper* 1, p. 36-45.
- Katsui, Yoshio, 1953, Petro-chemical study on the lavas from volcano Rishiri, Hokkaido, Japan: *Hokkaido Univ. Fac. Sci. Jour.*, ser. 4, v. 8, p. 245-258.
- Katsura, Takashi, 1956, Geochemical study of the volcanoes in Japan. (Part 33) Vanadium content in volcanic rocks of the Fuji volcanic zone: *Chem. Soc. Japan Jour.*, v. 77, p. 358-363.
- Kawano, Yoshinori, 1950, Natural glasses in Japan: *Japan Geol. Survey Rept.* 134, 29 p. (in Japanese).
- Kawano, Yoshinori, Yagi, Kenzo, Aoki, Ken-ichiro, 1961, Petrography and petrochemistry of the volcanic rocks of Quaternary volcanoes of northeastern Japan: *Tohoku Univ. Sci. Repts.*, ser. 3, v. 7, p. 1-46.
- Kennedy, G. C., 1955, Some aspects of the role of water in rock melts: in Poldervaart, Aric, ed., *Crust of the earth—a symposium*, *Geol. Soc. America Spec. Paper* 62, p. 489-503.
- Kuno, Hisashi, 1933, Preliminary note on basalt from Aziro, Idu: *Tokyo Imp. Univ. Earthquake Research Inst. Bull.*, v. 11, p. 391-401.
- 1935, Preliminary note on the occurrence of pigeonite as phenocrysts in some pyroxene andesite from Hakone volcano: *Geol. Soc. Japan Jour.*, v. 42, p. 39-44.
- 1936a, Chemical compositions of volcanic rocks from Izu and Hakone: *Volcanol. Soc. Japan Bull.*, v. 3, p. 53-71 (in Japanese).
- 1936b, Petrological notes on some pyroxene-andesites from Hakone volcano, with special reference to some types with pigeonite phenocrysts: *Japanese Jour. Geology Geography*, v. 13, p. 107-140.
- 1950a, Composite lava flows and dikes found in North Izu, Japan: *Geol. Soc. Japan Jour.*, v. 56, p. 167-172.
- 1950b, Petrology of Hakone volcano and the adjacent areas, Japan: *Geol. Soc. America Bull.*, v. 61, p. 957-1020.
- 1954, Geology and petrology of Ōmuro-yama volcano group, North Izu: *Tokyo Univ. Fac. Sci. Jour.*, sec. 2, v. 9, p. 241-265.
- 1960, High-alumina basalt: *Jour. Petrology*, v. 1, p. 121-145.
- 1962, Catalogue of the active volcanoes of the world including solfatara fields. Part XI. Japan, Taiwan, and Marianas: *Rome, Internat. Volcanolog. Assoc.*, 332 p.
- 1965, Fractionation trends of basalt magmas in lava flows: *Jour. Petrology*, v. 6, p. 302-321.
- Kushiro, Ikuo, 1964, The system diopside-forsterite-enstatite at 20 kilobars: *Carnegie Inst. Washington Year Book* 63, p. 101-108.
- Kushiro, Ikuo, and Schairer, J. F., 1963, New data on the system diopside-forsterite-silica: *Carnegie Inst. Washington Year Book* 62, p. 95-103.
- Lacroix, Alfred, 1923, *Minéralogie de Madagascar*, v. 3: Paris, Soc. d'Éd. Géol., Maritimes et Coloniales, 450 p.
- 1927, La constitution lithologique des îles volcaniques de la Polynésie australe: *Mém. L'Acad. Sci. L'Inst. France, Mem.* 2, v. 59, 82 p.
- MacKenzie, D. B., 1960, High-temperature alpine-type peridotite from Venezuela: *Geol. Soc. America Bull.*, v. 71, p. 303-318.
- Muan, Arnulf, 1955, Phase equilibria in the system $\text{FeO-Fe}_2\text{O}_3\text{-SiO}_2$: *Jour. Metals*, v. 7, September, Am. Inst. Mining Metall. Petroleum Engineers Trans., v. 203, p. 965-976.
- 1958, Phase equilibria at high temperatures in oxide systems involving changes in oxidation states: *Am. Jour. Sci.*, v. 256, p. 171-207.

- Muan, Arnulf, and Osborn, E. F., 1956, Phase equilibria at liquidus temperatures in the system $\text{MgO-FeO-Fe}_2\text{O}_3\text{-SiO}_2$: *Am. Ceramic Soc. Jour.*, v. 39, p. 121-140.
- , 1965, Phase equilibria among oxides in steelmaking: Reading, Mass., Addison-Wesley Publishing Co., 236 p.
- Muan, Arnulf, and Sōmiya, Shigeyuki, 1960, Phase equilibria in the system iron oxide- $\text{Cr}_2\text{O}_3\text{-SiO}_2$ in air: *Am. Ceramic Soc. Jour.*, v. 43, p. 531-541.
- Muir, I. D., Tilley, C. E., and Scoon, J. H., 1957, Contributions to the petrology of Hawaiian basalts. 1. The picrite-basalts of Kilauea: *Am. Jour. Sci.*, v. 255, p. 241-253.
- Murata, K. J. and Richter, D. H., 1966, The settling of olivine in Kilauean magma as shown by lavas of the 1959 eruption: *Am. Jour. Sci.*, v. 264, p. 194-203.
- Nagashima, Kozo, 1953, Geochemistry of the Kita-Izu and Hakone volcanic rocks, Shidara volcanic rocks, and Hamada nepheline basalts: Tokyo Univ. Agr. and Technol. Fac. Agr. Bull., v. 1, no. 2, p. 1-39.
- Nicholls, G. D., Nalwalk, A. J., and Hays, E. E., 1964, The nature and composition of rock samples dredged from the Mid-Atlantic Ridge between 22°N and 52°N: *Marine Geology*, v. 1, p. 333-343.
- Osborn, E. F., 1959, Role of oxygen pressure in the crystallization and differentiation of basaltic magma: *Am. Jour. Sci.*, v. 257, p. 609-647.
- , 1962a, Reaction series for subalkaline igneous rocks based on different oxygen pressure conditions: *Am. Mineralogist*, v. 47, p. 211-226.
- , 1962b, Addendum note to "Reaction series for subalkaline igneous rocks based on different oxygen pressure conditions": *Am. Mineralogist*, v. 47, p. 1480-1481.
- Osborn, E. F., and Muan, Arnulf, 1960, Phase equilibrium diagrams of oxide systems. Pl. 2. The system CaO-MgO-SiO_2 : Columbus, Ohio, Am. Ceramic Soc.
- Osborn, E. F., and Roeder, P. L., 1960, Effect of oxygen pressure on crystallization in simplified basalt systems: *Internat. Geol. Cong.*, 21st, Copenhagen 1960, Proc., sec. 13, pt. 13, p. 147-155.
- Osborn, E. F., and Schairer, J. F., 1941, The ternary system pseudowollastonite-akermanite-gehlenite: *Am. Jour. Sci.*, v. 239, p. 715-763.
- Parrish, William, 1953, Norelco instrument and operating manual: Irvington-on-Hudson, New York, North American Phillips Co.
- Phillips, Bert, and Muan, Arnulf, 1959, Phase equilibria in the system $\text{CaO-iron oxide-SiO}_2$ in air: *Am. Ceramic Soc. Jour.*, v. 42, p. 413-423.
- , 1960, Stability relations of calcium ferrites: phase equilibria in the system $2\text{CaO} \cdot \text{Fe}_2\text{O}_3\text{-FeO} \cdot \text{Fe}_2\text{O}_3\text{-Fe}_2\text{O}_3$ above 1135°C: *Metall. Soc. Am. Inst. Mining Metall. Petroleum Engineers Trans.*, v. 218, no. 6, p. 1112-1118.
- Phillips, Bert, Sōmiya, Shigeyuki, and Muan, Arnulf, 1961, Melting relations of magnesium oxide-iron oxide mixtures in air: *Am. Ceramic Soc. Jour.*, v. 44, p. 167-169.
- Powers, H. A., 1932, The lavas of the Modoc Lava-Bed quadrangle, California: *Am. Mineralogist*, v. 17, p. 253-294.
- Richardson, Constance, 1933, Petrology of the Galapagos Islands: *Bernice P. Bishop Mus. Bull.* 110, p. 45-67.
- Roeder, P. L., ms, 1960, Phase relations in the $\text{Mg}_2\text{SiO}_4\text{-CaAl}_2\text{Si}_2\text{O}_7\text{-FeO-Fe}_2\text{O}_3\text{-SiO}_2$ system and their bearing on crystallization of basaltic magma: Ph.D. thesis, The Pennsylvania State Univ., 105 p.
- Roeder, P. L., and Osborn, E. F., 1966, Experimental data for the system $\text{MgO-FeO-Fe}_2\text{O}_3\text{-CaAl}_2\text{Si}_2\text{O}_7\text{-SiO}_2$ and their petrologic implications: *Am. Jour. Sci.*, v. 264, p. 428-480.
- Ross, C. S., Foster, M. D., and Myers, A. T., 1954, Origin of dunites and of olivine-rich inclusions in basaltic rocks: *Am. Mineralogist*, v. 39, p. 693-737.
- Ruckmick, J. C., and Noble, J. A., 1959, Origin of the ultramafic complex at Union Bay, southeastern Alaska: *Geol. Soc. America Bull.*, v. 70, p. 981-1018.
- Sahama, Th. G., and Hytönen, Kai, 1958, Calcium-bearing magnesium-bearing olivines: *Am. Mineralogist*, v. 43, p. 862-871.
- Shepherd, E. S., Rankin, G. A., and Wright, F. E., 1909, The binary systems of alumina with silica, lime, and magnesia: *Am. Jour. Sci.*, 4th ser. v. 28, p. 293-333.
- Smith, C. H., and MacGregor, I. D., 1960, Ultrabasic intrusive conditions illustrated by the Mt. Albert ultrabasic pluton, Gaspé, Quebec [abs.]: *Geol. Soc. America Bull.*, v. 71, p. 1978.
- Snyder, G. L., 1959, Geology of Little Sitkin Island, Alaska: *U. S. Geol. Survey Bull.* 1028-H, p. 169-210.

- Sosman, R. B., 1952, Temperature scales and silicate research: *Am. Jour. Sci.*, Bowen v., p. 517-528.
- Speidel, D. H., ms, 1964, Element distribution among coexisting phases in the system $\text{MgO-FeO-Fe}_2\text{O}_3\text{-SiO}_2\text{-TiO}_2$ as a function of temperature, oxygen fugacity, and bulk composition: Ph.D. thesis, The Pennsylvania State Univ., 142 p.
- Swift, W. H., White, W. C., Wiles, J. W., and Worst, B. G., 1953, The geology of the lower Sabi coalfield: *Southern Rhodesia Geol. Survey Bull.* 40, 90 p.
- Taylor, H. P., Jr., and Epstein, S., 1963, $\text{O}^{18}/\text{O}^{16}$ ratios in rocks and coexisting minerals of the Skaergaard intrusion, East Greenland: *Jour. Petrology*, v. 4, p. 51-74.
- Taylor, H. P., Jr., and Noble, J. A., 1960, Origin of the ultramafic complexes in southeastern Alaska: *Internat. Geol. Cong.*, 21st, Copenhagen 1960, Proc., sec. 13, pt. 13, p. 175-187.
- Tilley, C. E., 1947, The dunite-mylonites of St. Paul's Rocks (Atlantic): *Am. Jour. Sci.*, v. 245, p. 483-491.
- Tsuya, Hiromichi, 1929, Volcanoes of Kôzu-shima: *Tokyo Univ. Earthquake Research Inst. Bull.*, v. 7, pt. 2, p. 269-334.
- 1935, On some lavas of volcano Huzi (Fuji): *Tokyo Imp. Univ. Earthquake Research Inst. Bull.*, v. 13, p. 646-659.
- 1937, On the volcanism of the Huzi volcanic zone, with special reference to the geology and petrology of Idu and the southern islands: *Tokyo Imp. Univ. Earthquake Research Inst. Bull.*, v. 15, p. 215-357.
- 1942, Secondary melting of basaltic ejecta by volcanic exhalations: *Tokyo Univ. Earthquake Research Inst. Bull.*, v. 20, p. 154-161.
- 1955, Geological and petrological studies of volcano, Fuji, V. 5. On the 1707 eruption of volcano Fuji: *Tokyo Univ. Earthquake Research Inst. Bull.*, v. 33, p. 341-384.
- Wager, L. R., 1960, The major element variation of the layered series of the Skaergaard intrusion and a re-estimation of the average composition of the hidden layered series and of the successive residual magmas: *Jour. Petrology*, v. 1, p. 364-398.
- Wager, L. R., and Deer, W. A., 1939, Geological investigations in East Greenland. Pt. 3. The petrology of the Skaergaard intrusion, Kangerdlugssuaq, East Greenland: *Medd. om Grønland*, v. 105, no. 4, 352 p.
- Washington, H. S., and Keyes, M. G., 1927, Rocks of the Galapagos Islands [and of Hawaii]: *Washington Acad. Sci. Jour.*, v. 17, p. 538-543.
- Yoder, H. S., Jr., and Sahama, Th. G., 1957, Olivine X-ray determinative curve: *Am. Mineralogist*, v. 42, p. 475-491.
- Yoder, H. S., Jr., and Tilley, C. E., 1962, Origin of basalt magmas: an experimental study of natural and synthetic rock systems: *Jour. Petrology*, v. 3, p. 342-532.